MNRAS 000, 1–17 (2020) Preprint 6 February 2020 Compiled using MNRAS LATEX style file v3.0

Survey of Gravitationally-lensed Objects in HSC Imaging (SuGOHI). V. Group-to-cluster scale lens search from the HSC-SSP Survey

Anton T. Jaelani[1,2,3]★, Anupreeta More[4,5], Masamune Oguri[4,6,7], Alessandro Sonnenfeld[4,8], Sherry H. Suyu[9,10,11], Cristian E. Rusu[12], Kenneth C. Wong[4], James H. H. Chan[13], Issha Kayo[14], Chien-Hsiu Lee[15], Dani C. -Y. Chao[9,10], Jean Coupon[16], Kaiki T. Inoue[1], and Toshifumi Futamase[17]

[1]*Department of Physics, Kindai University, 3-4-1 Kowakae, Higashi-Osaka, Osaka 577-8502, Japan*
[2]*Astronomical Institute, Tohoku University, 6-3 Aramaki, Aoba-ku, Sendai 980-8578, Japan*
[3]*Astronomy Study Program and Bosscha Observatory, FMIPA, Institut Teknologi Bandung, Jl. Ganesha 10, Bandung 40132, Indonesia*
[4]*Kavli Institute for the Physics and Mathematics of the Universe (IPMU), 5-1-5 Kashiwanoha, Kashiwa-shi, Chiba 277-8583, Japan*
[5]*The Inter-University Centre for Astronomy and Astrophysics (IUCAA), Post Bag 4, Ganeshkhind, Pune 411007, India*
[6]*Department of Physics, The University of Tokyo, 7-3-1 Hongo, Bunkyo-ku, Tokyo 113-0033, Japan*
[7]*Research centre for the Early Universe (RESCEU), The University of Tokyo, 7-3-1 Hongo, Bunkyo-ku, Tokyo 113-0033, Japan*
[8]*Leiden Observatory, Leiden University, Niels Bohrweg 2, 2333 CA Leiden, the Netherlands*
[9]*Max-Planck-Institut für Astrophysik, Karl-Schwarzschild-Straße 1, 85748 Garching, Germany*
[10]*Physik-Department, Technische Universität München, James-Franck-Straße 1, 85748 Garching, Germany*
[11]*Academia Sinica Institute of Astronomy and Astrophysics (ASIAA), 11F of ASMAB, No. 1, Section 4, Roosevelt Road, Taipei 10617, Taiwan*
[12]*Subaru Telescope, National Astronomical Observatory of Japan, 2-21-1 Osawa, Mitaka, Tokyo 181-0015, Japan*
[13]*Laboratory of Astrophysique, École Polytechnique Fédérale de Lausanne (EPFL), Observatoire de Sauverny, 1290 Versoix, Switzerland*
[14]*Department of Liberal Arts, Tokyo University of Technology 5-23-22 Nishikamata, Ota-ku, Tokyo 144-8650, Japan*
[15]*National Optical Astronomy Observatory 950 N Cherry Avenue, Tucson, AZ 85719, USA*
[16]*Department of Astronomy, University of Geneva, ch. d'Écogia 16, 1290 Versoix, Switzerland*
[17]*Department of Astrophysics and Atmospheric Sciences, Kyoto Sangyo University, Kyoto, Kyoto 603-8555, Japan*

Accepted XXX. Received YYY; in original form ZZZ

ABSTRACT

We report the largest sample of candidate strong gravitational lenses belonging to the Survey of Gravitationally-lensed Objects in HSC Imaging for group-to-cluster scale (SuGOHI-c) systems. These candidates are compiled from the S18A data release of the Hyper Suprime-Cam Subaru Strategic Program (HSC-SSP) Survey. We visually inspect ∼ 39,500 galaxy clusters, selected from several catalogs, overlapping with the Wide, Deep, and UltraDeep fields, spanning the cluster redshift range $0.05 < z_{\rm cl} < 1.38$. We discover 641 candidate lens systems, of which 537 are new. From the full sample, 47 are almost certainly bonafide lenses, 181 of them are highly probable lenses and 413 are possible lens systems. Additionally, we present 131 lens candidates at galaxy-scale serendipitously discovered during the inspection. We obtained spectroscopic follow-up of 10 candidates using the X-shooter. With this follow-up, we confirm 8 systems as strong gravitational lenses. Out of the remaining two, the lensed sources of one of them was too faint to detect any emission, and the source in the second system has redshift close to the lens but other additional arcs in this system are yet to be tested spectroscopically. Since the HSC-SSP is an ongoing survey, we expect to find ∼ 600 definite or probable lenses using this procedure and more if combined with other lens finding methods.

Key words: gravitational lensing: strong – galaxies: clusters: general – surveys – methods: observational

1 INTRODUCTION

Standard model of cosmology suggests that the Universe is dominated by dark matter and dark energy. Strong gravitational lensing is a phenomenon where multiply lensed images of distant sources can be seen due to deflection by gravity of the intervening massive

★ E-mail: anton@phys.kindai.ac.jp

objects such as galaxies and galaxy clusters. Gravitational lensing has been shown to be a promising technique to probe these dark components. Lensing has been used to study distant galaxies with extreme magnification (e.g., Swinbank et al. 2009; Zitrin & Broadhurst 2009; Richard et al. 2011), substructure in the lensing halos (e.g., More et al. 2009; Vegetti et al. 2010a,b; Hezaveh et al. 2016), tighter constraints on the Hubble constant (e.g., Suyu et al. 2010; Bonvin et al. 2017; Wong et al. 2019) and constraints on the slope of the inner density profile of the lensing halos (e.g., Koopmans & Treu 2003; Koopmans et al. 2006; More et al. 2008; Barnabè et al. 2009; Koopmans et al. 2009).

This has motivated, dedicated efforts in searching for gravitational lenses from large astronomical surveys e.g., the Hyper Suprime-Cam Subaru Strategic Program (HSC-SSP) Survey (Aihara et al. 2018a), DESI Legacy Imaging Surveys (Dey et al. 2019), Kilo Degree Survey (KiDS, de Jong et al. 2015), and Dark Energy Survey (DES, Dark Energy Survey Collaboration et al. 2016). Specifically, large imaging and spectroscopic surveys have allowed inferences of statistical properties of lenses such as constraints on the stellar initial mass function (e.g., Treu et al. 2010; Ferreras et al. 2010; Sonnenfeld et al. 2012, 2019) or estimation of the fraction of dark matter in galaxy-scale halos ((e.g., Gavazzi et al. 2007; Grillo 2010; Faure et al. 2011; Ruff et al. 2011; More et al. 2011) or even cosmology (e.g., Gladders et al. 2003; Oguri et al. 2012).

As mentioned above, most of the surveys have primarily focused on studying galaxy-scale or cluster-scale structures. As a result, matter distribution in galaxies and galaxy clusters is relatively well-studied via both strong and weak lensing. A further improvement in our understanding has come from the use of complementary methods to lensing such as stellar kinematics, satellite kinematics and X-ray scaling relations. In contrast, there has not been much progress (in the last decade) on mass distributions of galaxy groups, in the mass range of $10^{12} - 10^{14} M_{\odot}$, intermediate to galaxies and galaxy clusters. Using X-ray sample to study the intragroup medium at low redshifts (Helsdon & Ponman 2000), mass-to-light ratios of groups from the Canadian Network for Observational Cosmology 2 (CNOC 2) sample (e.g., Parker et al. 2005), faint end of the luminosity function of nearby compact groups (e.g., Krusch et al. 2006), concentration-mass ($c - M$) relation of groups (e.g., Mandelbaum et al. 2008; Newman et al. 2015), colours and star formation of galaxy groups (e.g., Balogh et al. 2009, 2011), scaling relations of X-ray selected groups (Rines & Diaferio 2010) and baryon fractions from the Two Micron All Sky Survey (2MASS) (Dai et al. 2010) are some examples of investigations of galaxy groups.

We still do not have a detailed understanding of matter distribution, formation and evolution of galaxy groups. Being one of the important components in the hierarchical assembly of structures in the Universe, galaxy groups are much more massive than galaxy-scale halos and are concentrated enough to act as lenses. Furthermore, since galaxy groups are quite abundant compared to massive structures like galaxy clusters, the probability of finding group-scale lenses is also large. Hence, strong lensing can be successfully used to study group-scale halos (Limousin et al. 2009; More et al. 2012; Foëx et al. 2013, 2014; Verdugo et al. 2014; Newman et al. 2015).

In this work, we conduct a systematic search of group- and cluster-scale lenses which is part of the Survey of Gravitationally-lensed Objects in HSC Imaging (SuGOHI) and also present results of spectroscopic follow-up of a sub-sample. The galaxy-scale lens sample (SuGOHI-g) is presented in Sonnenfeld et al. (2018, 2019) and Wong et al. (2018), and results of search for lensed quasars (SuGOHI-q) are reported in Chan et al. (2019). This paper is organised as follows. In Section 2, we describe the HSC-SSP imaging data used in our search. In Section 3, we describe the procedure for finding new strong gravitational lens systems. We present our newly discovered lens candidates in Section 4. In Section 5, we describe our spectroscopic follow-up observation. We present our summary and conclusion in Section 6.

Table 1. Clusters found in the HSC-SSP S18A footprint from different algorithms, some of which are external to the HSC Survey collaboration.

Catalog	Catalog label	Number of Clusters
CAMIRA	CAM	14,992
Ford et al. (2015)	F	9,475
Rykoff et al. (2016)	R	2,968
Wen et al. (2012)	W	12,000

2 THE DATA

The Subaru Strategic Program (SSP) survey is carried out with the Hyper Suprime-Cam (HSC, Miyazaki et al. 2018; Komiyama et al. 2018; Kawanomoto et al. 2018; Furusawa et al. 2018; Huang et al. 2018; Coupon et al. 2018), a 1.7 deg^2 field-of-view optical camera recently installed on the Subaru 8.2m telescope. The HSC-SSP Survey has three fields; the Wide field is expected to cover a 1,400 deg^2 area in five bands (g, r, i, z, and y) to an i-band depth of 26.2 by its completion, while the Deep+UltraDeep fields are expected to cover smaller areas of about 27 deg^2 and 3.5 deg^2, respectively (see Aihara et al. (2018a) for more details about the survey). We use the photometric data from the S18A data release, which covers 1,114 deg^2 (out of which 305 deg^2 is full depth) in Wide and 31 deg^2 in Deep+UltraDeep, at least in one filter and one exposure (Aihara et al. 2019). The data are processed with the reduction pipeline HSCPIPE v6.7 (Bosch et al. 2018), a version of the Large Synoptic Survey Telescope stack (Axelrod et al. 2010; Jurić et al. 2017; Ivezić et al. 2008, 2019). The median seeing of S18A data is 0.61″ in the i-band, 0.85″ in the g-band and the pixel scale of HSC is 0.168″.

The redshifts used in this work are obtained from the photometric redshift catalog of the HSC-SSP Survey, determined using the Direct Empirical Photometric code (DEmP, Hsieh & Yee 2014). The HSC-SSP photometric redshifts are the most accurate at $0.2 \lesssim z_{\rm phot} \lesssim 1.5$. The point estimates of the photometric redshift are accurate to better than 1% in term of $\langle \Delta z/(1+z) \rangle$ with scatter of ≈ 0.04 and an outlier rate of $\approx 8\%$ for galaxies with $i < 24$ mag. A more detailed description of DEmP's application to the HSC-SSP data is presented in Tanaka et al. (2018). Since the HSC-SSP Survey footprint has some overlap with that of the Sloan Digital Sky Survey (SDSS), we also extracted spectroscopic redshifts, whenever available, from the SDSS Data Release 15 (Aguado et al. 2019) catalogs.

3 LENS CANDIDATE SELECTION

In this section, we describe how the cluster catalogs are selected for visual inspection and our criteria to grade the lens candidates. We used the HSCMAP (SKY EXPLORER), an online tool, to visually inspect colour images of the clusters (see Section 3.1). The lens search relied on morphology and colour information to visually analyse properties of the lensed images and the galaxies in the cluster to assess the plausibility of lensing. Inspectors could control

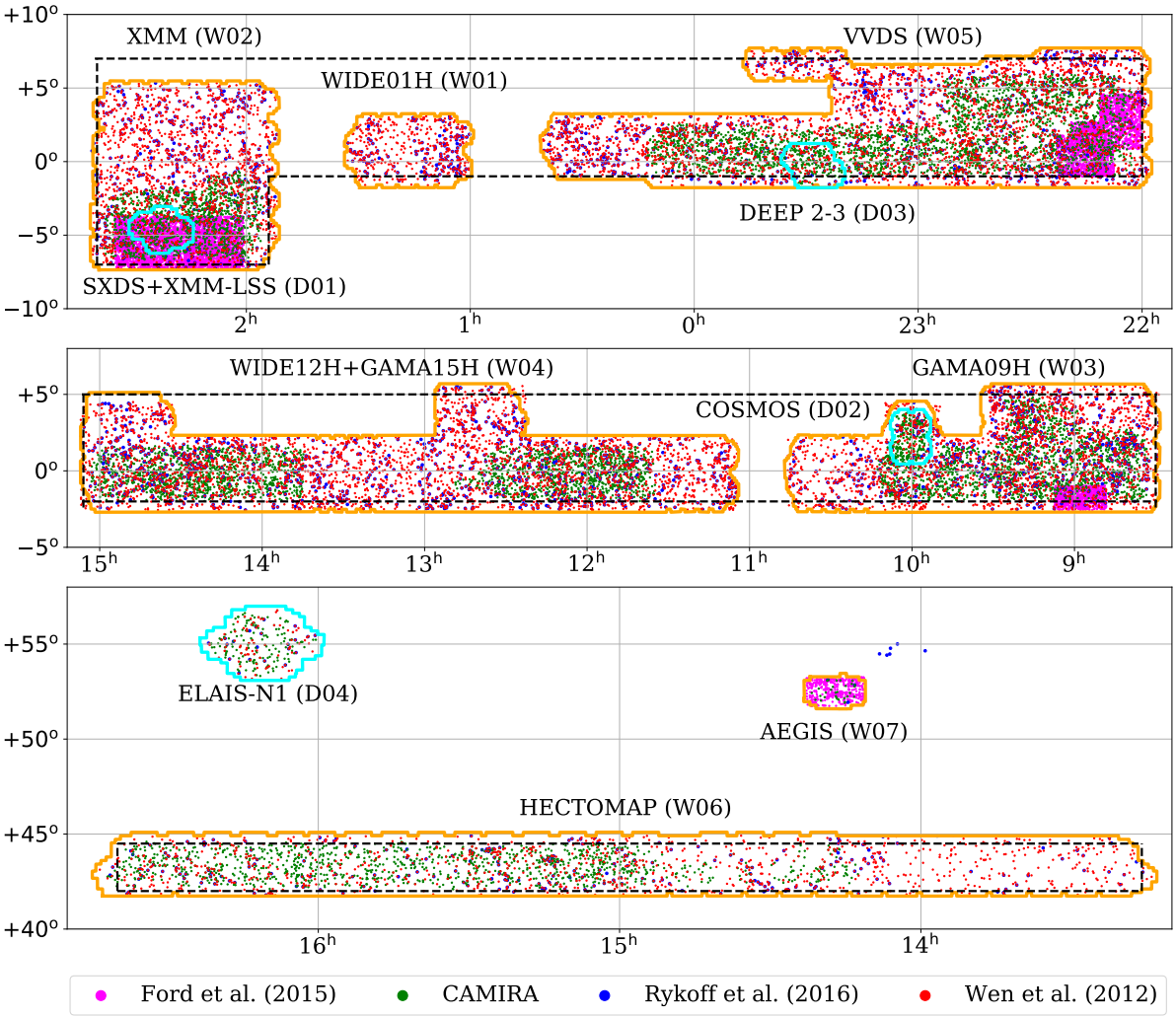

Figure 1. The Hyper Suprime-Cam Subaru Strategic Program (HSC-SSP) observational footprint shown in equatorial coordinates. The orange and cyan boxes indicate the Wide and Deep+UltraDeep fields for S18A data release (internal), respectively. The dashed black boxes indicate the approximate boundaries of the three disjoint regions that will make up the final Wide survey. The overlapping cluster catalogs are shown by different point colours.

the spatial scales, contrast and brightness and could choose different combinations of the HSC filters.

3.1 Parent Catalogs

We used galaxy cluster catalogs which have been run on the footprint covering the HSC-SSP S18A imaging. The on-sky distribution of these clusters, along with survey footprints, is shown in Figure 1. We also give the number of clusters detected from each of the four catalogs in Table 1.

3.1.1 Clusters from the HSC-SSP Survey

Our primary cluster catalog is called CAMIRA which is produced by running the cluster-finding algorithm (Oguri 2014) on the internal HSC-SSP data release S18A[1] (Aihara et al. 2019), covering roughly 465 deg^2 and 28 deg^2, in all five filters, for Wide and Deep+UltraDeep fields, respectively. The CAMIRA is validated through comparisons with existing spectroscopic and X-ray data as well as mock galaxy catalogs.

We obtain 14,992 clusters, comprising of 14,350 clusters from the Wide fields and 642 clusters from the Deep fields, with the richness limit $N_{\mathrm{ric,CAMIRA}} > 10$ spanning a redshift range of $0.1 < z_{\mathrm{cl}} < 1.38$. Richness in CAMIRA is defined to be the number of red member galaxies with stellar mass $M_{\mathrm{star}} \geq 10^{10.2} M_{\odot}$ lying within a physical radius of ≈ 1.4 Mpc. The richness limit $N_{\mathrm{ric,CAMIRA}} = 10$ corresponds to $M_{200} \approx 7 \times 10^{13} M_{\odot}$, where M_{200} is the cluster mass within r_{200}, by extrapolating the richness-mass relation of CAMIRA from Murata et al. (2019). The r_{200} is the radius within which the mean density of a cluster is 200 times of the critical density of the Universe. The cluster sample is shown by green points in Figure 1. The CAMIRA cluster catalog is still being constructed from the HSC-SSP Survey data, since the HSC survey is an ongoing and several patches are likely to have incomplete imaging data, e.g., has ≤ 4 filters. As a result, we decided to make use of other public catalogs constructed from previous surveys which have overlapped with the HSC-SSP Survey footprint, e.g., the Sloan Digital Sky

[1] Note that the currently published CAMIRA catalog makes use of the data release S16A only and it can be obtained from Oguri et al. (2018). However, this is a subsample of the catalog used in our study.

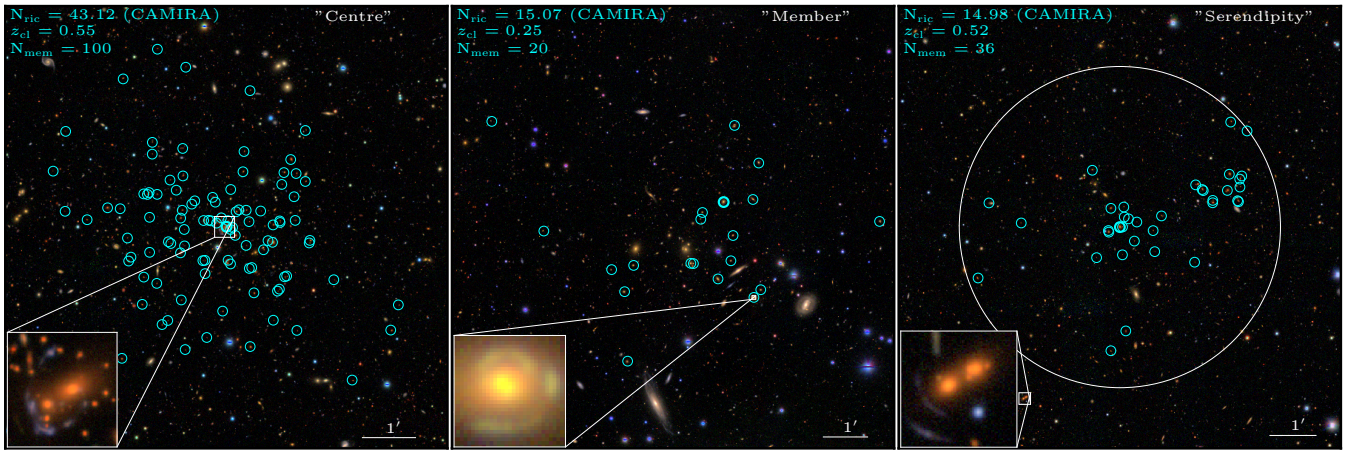

Figure 2. Types of lens candidates depending on their location with respect to galaxy clusters. Lens candidates where the BCG acts as a lens (**left panel**, e.g., HSC J1441−0053) or a member galaxy (see more description in Section 4) acts as a lens (**middle panel**, e.g., HSC J2233+0157) are classified as SuGOHI-g, otherwise as serendipity (**right panel**, e.g., HSC J1414−0136). The cyan circles indicate member galaxies of a cluster and the brightest cluster galaxy (BCG) is indicated by thicker circle. The white circle indicates a region which covered member galaxies with the BCG as the centre. The richness $N_{\rm ric}$, cluster redshift $z_{\rm cl}$, and number of galaxy member $N_{\rm mem}$, are shown on the top left.

Survey (SDSS, York et al. 2000) and the Canada-France Hawaii Telescope Lensing Survey (CFHTLenS, Heymans et al. 2012). Also, including more cluster catalogs maximises the chance of finding more group-to-cluster scale lenses.

3.1.2 *Clusters from Data Release 8 of SDSS-III Data*

The HSC-SSP Survey footprint has almost complete overlap with SDSS footprint. We thus have two extensive cluster catalogs, Wen et al. (2012) and Rykoff et al. (2016), that can be used. Both catalogs are derived from the galaxy data of 14,000 deg^2 of SDSS-III (Eisenstein et al. 2011). Wen et al. (2012) identified 132,684 clusters (12,000 of them overlap with the HSC-SSP S18A footprint, see Table 1 and red points in Figure 1) in the redshift range of $0.05 \leq z_{\rm cl} < 0.8$. The clusters are selected if their richness $N_{\rm ric,Wen} \geq 12$ which corresponds to $M_{200} \approx 0.6 \times 10^{14} M_\odot$ and a number of member galaxies candidates $N_{200} \geq 8$ within r_{200}. We also used clusters from the red-sequence Matched-filter Probabilistic Percolation (REDMAPPER, for the details see Rykoff et al. 2014) cluster finding algorithm (version 6.3). This catalog has a total of 25,236 clusters (2,968 are overlapping with the HSC-SSP S18A footprint, see Table 1 and blue points in Figure 1) clusters in the redshift range $0.08 \leq z_{\rm cl} < 0.55$ with $N_{\rm ric,REDMAPPER} \geq 20$ which correspond to $M_{200} \gtrsim 10^{14} M_\odot$. For more detailed description of the catalog, please see in Rykoff et al. (2016).

3.1.3 *CFHTLenS Data*

Ford et al. (2015) has a sample of 18,056 clusters (9,475 of them overlap with the HSC-SSP S18A footprint, see Table 1) at redshifts $0.2 \leq z_{\rm cl} \leq 0.9$. The clusters have been detected using the 3D-Matched-Filter Galaxy Cluster Finder in the ~ 154 deg^2 CFHTLenS survey (Milkeraitis et al. 2010; Ford et al. 2014) with a significance ≥ 3.5 and richness $N_{\rm ric,Ford} > 2$ which correspond to $M_{200} \approx 6 \times 10^{12} M_\odot$. This field has a substantial overlap with the S18A data (see magenta points in Figure 1).

Table 2. Lens candidate statistics. "CAM F R W" represent the parent cluster catalogs as presented in Table 1.

	Grade			Total	Known
	A	B	C		
SuGOHI-c	47	181	413	641	104
CAM	21	128	202	351	67
F	5	15	40	60	20
R	20	56	136	212	40
W	26	79	194	299	58
Serendipity	6	24	61	91	12

3.2 Ranking criteria

We identified 39,435 clusters, located in the HSC-SSP S18A footprint, from the four catalogs combined. Inspectors use the online HSCMAP (SKY EXPLORER) server to inspect colour images of the clusters (Aihara et al. 2018b, 2019). In the first step, we divided the clusters into three redshift bins which were inspected by three inspectors per redshift bin. After we compiled the 1160 candidates from all redshift bins combined, nine inspectors independently assigned a rank from 0 to 3, according to the following criteria

- 3: almost certainly a lens,
- 2: probably a lens,
- 1: possibly a lens, and
- 0: not a lens.

We further refined the sample of candidates by applying the following scheme:

A: $\langle$Rank$\rangle > 2.5$,
B: $1.5 < \langle$Rank$\rangle \leq 2.5$,
C: $0.5 < \langle$Rank$\rangle \leq 1.5$, and
Not: else.

where $\langle$Rank$\rangle$ is the mean rank estimated from the ranks given by individual inspectors. The sample, thus, consists of 772 candidates. The systems with highly discrepant ranks were discussed and regraded to mitigate such discrepancies.

4 RESULTS

The Einstein radius, $\theta_{\rm Eins}$, is the best parameter to represent mass of the lens which can be approximated from the arc radius, $R_{\rm arc} \approx 2\theta_{\rm Eins}$ (More et al. 2012). Typically, lensing halos with Einstein radius larger than $\geq 2''$ are very massive lenses with significant contribution from the environment of the primary lensing galaxy (Oguri 2006; More et al. 2012). Here, we calculated the arc radius by assuming a circle which covered mostly the candidate arc with the Brightest Cluster Galaxy (BCG) as the centre.

Next, we classified the graded systems into two: SuGOHI-c and additional lenses at galaxy-scale (SuGOHI-g, see Appendix A), which are shown by Table 3 and Table A2, respectively. The classification criteria for a candidate to be included in SuGOHI-c are the following:

1. If the lensing is due to the brightest central galaxy (BCG) (see the left panel in Figure 2), and
2. either the angular separation of the arc from the lens centre, the arc radius, $R_{\rm arc} \geq 2''$ (e.g., HSC J1557+4206),
3. or if the lensing is caused by more than one galaxy enclosed by a ring through the arc or multiple images (e.g., HSC J2228+0022).

If none of the above is satisfied, candidates fall in the SuGOHI-g sample which are serendipitously discovered during the inspection (e.g., HSC J0904+0102 (Jaelani et al. 2019), which has a similar position with HSC J1414+0136 respect to the cluster position (see right panel of Figure 2)), and are reported in the Appendix.

For the first classification criteria, if a BCG is misclassified[2] to be a member galaxy by the algorithm, only then we accept it as a SuGOHI-c system. A member galaxy may be aided by the group potential, but then the arc separation also needs to be $R_{\rm arc} \geq 2''$ (see the middle panel in Figure 2). Otherwise, this could still be a galaxy-scale lens. In some rare cases, an arc radius cannot be quite quantified because it is being deflected by multiple galaxies on either side (e.g., see HSC J0209−0448, grade C in the online material[3]). These are also included as SuGOHI-c.

A total of 641 systems (including 537 new lenses presented for the first time) are in the SuGOHI-c sample. These consist of 47 Grade A, 181 Grade B, and 413 Grade C systems, respectively. We found some candidate systems in more than one catalog that are shown in Figure 3. The CAMIRA has the largest number which corresponds to candidate systems. We also found many candidates serendipitously which were missed by parent cluster catalogs. Some of these lenses were also discovered independently by citizen scientists project (SPACE WARPS, Marshall et al. 2016; More et al. 2016) from the HSC-SSP Survey (Sonnenfeld et al., in prep). We present the lens candidate statistics in Table 2.

We provide the full candidate systems of the SuGOHI-c in the online material[3]. The list of SuGOHI-c with grades A and B is presented in Table 3 which provides the system name, the equatorial coordinates, the lens and source redshift, the arc radius, the mean and the σ of the rank, a qualitative grade, the parent catalog, and references from previous studies. Figures 4 show composite colour (*gri* or *riz*) cutouts of grades A and B for the SuGOHI-c sample. At the top of each cutout is the system name. At the bottom left is a grade (labeled "A" or "B"), as well as a label "K" if the lens is previously known. The known candidates have been identified

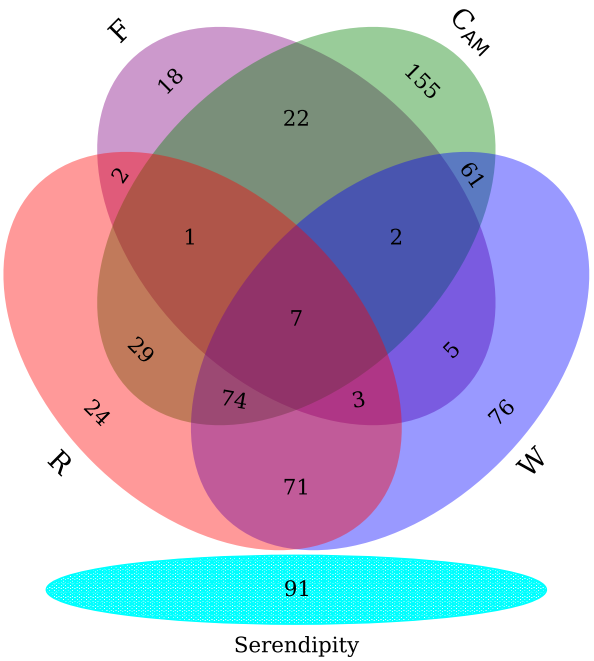

Figure 3. Distribution of lens candidates according to the parent cluster catalogs. The letters represent the parent cluster catalogs as presented in Table 1. The Venn diagram is divided into two panels: 550 lens systems of SuGOHI-c correspond to the parent cluster (upper) and 91 lens systems which serendipiously (bottom) discovered during the inspection, thus, not listed as BCGs of the clusters or not even members with $R_{\rm arc} \geq 2''$.

by cross-matching with the published systems in the literature, as reported in Table 3.

We show the photometric redshift distribution of lens galaxies and arc radii of the systems in Figure 5, and for comparison, we also show 125 lens systems of the SARCS sample distribution with $R_{\rm arc} \geq 2''$ from More et al. (2012). We find that the mean of the lens redshift for the SuGOHI-c sample and SARCS sample are $z = 0.50 \pm 0.23$ and $z = 0.58 \pm 0.22$, respectively. We note that the mean redshifts of both samples have good agreement.

During our inspection, we also found a number of strong lens systems with red-coloured sources (e.g., HSC J0211−0343, HSC J1143+0102). We mark such a system with a † in Table 3. Some of them are high redshift galaxies at $z_\ell \sim 6$ (Oguri et al., in prep and Ono et al., in prep). We further note that HSC J2211−0008 has a spectroscopically confirmed lensed source which is a Lyman Break Galaxy at $z = 2.26$. Details of the follow-up Subaru observations and analysis of this system will be reported in More et al. (in prep).

5 SPECTROSCOPIC FOLLOW-UP

We carried out spectroscopic observations of 10 candidates from SuGOHI-c sample in order to confirm the lensing nature and obtain spectroscopic redshifts essential for detailed mass modelling of strong lenses (Jaelani et al., in prep.). Our sample was part of the larger spectroscopic campaign for SuGOHI lenses (ESO programme 099.A-0220, PI: S. Suyu) with the Very Large Telescope (VLT)'s X-shooter. These candidates were selected from an early sample of grade A-B lenses with $z_\ell > 0.6$ from a smaller footprint. X-shooter is an Echelle spectrograph (Vernet et al. 2011), with an allowed wavelength range $\lambda\lambda$3,000 - 25,000 Å . The spectra are

[2] A BCG is considered to be misclassified if it is visually much brighter than its neighbours and/or the galaxy labelled as BCG by the cluster-finding algorithm.

[3] http://www-utap.phys.s.u-tokyo.ac.jp/~oguri/sugohi/

Table 3. SuGOHI-c candidates, with grades A and B, selected by visual inspection of galaxy cluster catalogs. Redshifts are DEmP photometric and SDSS DR15 spectroscopic redshifts. PC indicates the parent cluster catalog through which a candidate was selected as in Table 1. Systems with † and X are the lens candidates which have red-coloured sources and X-shooter follow-up, respectively. Systems with references are previously known, whereas other objects with "..." are new. References: [1]Diehl et al. (2017), [2]Huang et al. (2019), [3]Jacobs et al. (2019), [4]Petrillo et al. (2019), [5]Sonnenfeld et al. (2018), [6]Wong et al. (2018), [7]More et al. (2012), [8]More et al. (2016), [9]Cabanac et al. (2007), [10]Stark et al. (2013), [11]Tanaka et al. (2016), [12]Bolton et al. (2008), [13]Faure et al. (2008), [14]Hammer (1991), [15]Carrasco et al. (2017),[16]Chan et al. (2019),[17]Tyson et al. (1990).

Name	α(J2000)	δ(J2000)	$z_{\ell,\mathrm{phot}}$	$z_{\ell,\mathrm{spec}}$	R_{arc} (arcsec)	Rank	σ_{Rank}	Grade	PC	References
HSC J0003+0054	0.8045	0.9069	1.13	···	3.22	1.78	0.63	B	CAM	···
HSC J0004−0103	1.2155	−1.0551	0.48	···	3.23	2.78	0.42	A	···	1,15
HSC J0008+0015	2.2032	0.2641	0.40	0.397	2.57	2.75	0.46	A	···	···
HSC J0014−0057	3.7257	−0.9525	0.55	0.535	13.79	2.25	0.46	B	W	···
HSC J0032+0100	8.0733	1.0102	0.37	0.390	6.48	2.88	0.35	A	RW	···
HSC J0034+0225	8.6173	2.4227	0.32	···	13.01	2.75	0.46	A	RW	15
HSC J0107+0117†	16.7886	1.2918	0.44	0.422	9.64	2.00	0.47	B	W	2
HSC J0112−0022	18.1073	−0.3798	0.50	0.466	2.09	1.75	0.46	B	···	···
HSC J0156−0424	29.2265	−4.4071	0.12	···	3.03	2.44	0.50	B	CAMRW	···
HSC J0157−0515	29.3186	−5.2537	0.53	0.560	2.98	2.29	0.45	B	CAM	···
HSC J0159−0358	29.9093	−3.9829	1.11	···	4.38	2.29	0.45	B	CAM	···
HSC J0208−0237	32.0673	−2.6233	0.53	0.514	7.41	2.14	0.83	B	CAMRW	···
HSC J0209−0643	32.3721	−6.7200	0.40	0.407	3.08	2.67	0.67	A	FW	3,7
HSC J0210−0038	32.6662	−0.6422	0.24	0.287	5.72	1.63	0.74	B	RW	···
HSC J0211−0343†	32.8150	−3.7299	0.75	···	3.98	3.00	0.00	A	CAMF	···
HSC J0214−0206	33.5333	−2.1081	0.67	···	3.00	2.11	0.74	B	···	3
HSC J0214−0535	33.5335	−5.5925	0.47	0.445	6.37	2.86	0.35	A	CAMFRW	7,9
HSC J0217+0033	34.3360	0.5536	0.36	0.381	5.04	1.88	0.84	B	RW	···
HSC J0218−0515	34.5306	−5.2601	0.56	0.649	2.61	1.57	0.90	B	CAM	7,9
HSC J0219−0527	34.9850	−5.4665	0.29	0.285	3.00	2.44	0.73	B	CAMFW	7,9
HSC J0220−0222	35.1766	−2.3668	0.60	0.546	3.99	2.14	0.64	B	CAM	5
HSC J0222−0222	35.5932	−2.3699	1.18	···	3.18	1.67	0.67	B	CAM	···
HSC J0222−0258	35.7480	−2.9743	0.46	···	2.12	1.57	0.50	B	CAM	···
HSC J0224−0346	36.0040	−3.7738	0.95	···	2.56	1.86	0.64	B	CAM	7
HSC J0224−0336X	36.0437	−3.6015	0.61	0.613	3.89	2.29	0.45	B	CAMW	5
HSC J0225−0532	36.3888	−5.5346	0.58	0.566	3.98	1.56	0.73	B	CAMF	8
HSC J0228−0212	37.0118	−2.2005	0.23	0.206	3.76	2.29	0.45	B	CAMRW	···
HSC J0230−0540	37.5355	−5.6774	0.46	0.498	2.26	1.57	0.50	B	CAMF	8
HSC J0230−0159	37.7006	−1.9841	1.10	···	4.50	1.56	0.68	B	CAM	···
HSC J0231−0621	37.7516	−6.3612	1.17	···	2.18	3.00	0.00	A	CAM	···
HSC J0232−0323	38.2078	−3.3905	0.46	0.450	3.77	3.00	0.00	A	CAM	1,2,3,10
HSC J0233−0228	38.2734	−2.4769	0.61	0.572	4.99	2.71	0.45	A	CAM	···
HSC J0233−0328	38.3837	−3.4671	1.12	···	4.17	1.71	1.03	B	CAM	···
HSC J0235−0634	38.9092	−6.5684	0.20	0.181	2.13	2.00	0.00	B	CAMW	5
HSC J0236−0332	39.1554	−3.5389	0.28	0.269	2.12	3.00	0.00	A	CAMRW	5
HSC J0238−0348	39.5988	−3.8036	0.29	0.322	4.29	1.63	0.52	B	RW	···
HSC J0239−0127	39.9260	−1.4632	0.35	···	4.26	2.33	0.47	B	···	2
HSC J0239−0134	39.9714	−1.5827	0.37	0.373	10.86	2.88	0.35	A	RW	3,14
HSC J0837+0156	129.3593	1.9441	0.39	0.396	2.67	2.29	0.45	B	CAMR	4,5
HSC J0838+0208	129.7372	2.1474	0.36	0.360	6.95	1.56	0.54	B	CAMRW	···
HSC J0839−0140†	129.8890	−1.6792	0.28	···	2.43	2.56	0.68	A	W	···
HSC J0839+0228	129.9141	2.4756	0.42	0.431	3.87	1.56	0.68	B	CAM	···
HSC J0840+0135	130.2476	1.5970	0.56	0.550	3.42	1.56	0.50	B	CAMR	···
HSC J0844−0010	131.1135	−0.1832	0.37	···	4.62	1.56	0.50	B	CAMRW	···
HSC J0845−0054	131.3341	−0.9156	0.41	···	7.70	1.71	0.70	B	CAMRW	4
HSC J0846−0154	131.6363	−1.9049	1.03	···	3.93	1.67	0.67	B	CAM	···
HSC J0846+0446	131.6978	4.7679	0.23	0.241	4.41	1.75	0.71	B	RW	10
HSC J0852+0025	133.1269	0.4203	0.29	···	9.26	2.29	0.70	B	R	···
HSC J0854−0121	133.6944	−1.3607	0.34	···	5.02	2.88	0.35	A	FRW	4,9
HSC J0855+0024	133.9344	0.4105	0.56	···	3.45	1.57	0.50	B	CAMRW	···
HSC J0856+0125	134.0864	1.4174	0.68	0.719	2.60	2.29	0.70	B	CAM	5
HSC J0904+0125X	136.0180	1.4208	0.91	···	5.20	2.29	0.45	B	CAM	···
HSC J0904+0426	136.1276	4.4466	0.32	0.457	4.54	3.00	0.00	A	W	···
HSC J0906+0119	136.5461	1.3308	0.65	0.605	3.82	1.67	0.47	B	···	···
HSC J0907+0057X	136.9767	0.9587	0.72	···	7.00	2.29	0.70	B	CAM	···
HSC J0908+0119	137.0261	1.3319	0.69	0.659	5.08	1.67	0.47	B	CAMW	···
HSC J0909+0405	137.2978	4.0883	0.81	···	2.41	1.57	0.50	B	CAM	···
HSC J0912+0415	138.1252	4.2654	0.44	0.453	2.26	1.56	0.68	B	CAMW	···
HSC J0913+0352†	138.3040	3.8705	0.47	0.456	2.37	1.57	0.90	B	CAMR	···

Table 3. *Continued.*

Name	α(J2000)	δ(J2000)	$z_{\ell,\mathrm{phot}}$	$z_{\ell,\mathrm{spec}}$	R_{arc} (arcsec)	Rank	σ_{Rank}	Grade	PC	References
HSC J0919+0336	139.7692	3.6107	0.45	0.444	2.15	3.00	0.00	A	CamRW	5
HSC J0921+0214	140.4025	2.2363	0.33	0.319	2.15	2.29	0.45	B	CamW	4
HSC J0922+0259	140.6465	2.9950	1.10	···	2.15	2.33	0.50	B	Cam	···
HSC J0925+0226	141.2609	2.4362	0.39	0.390	4.66	1.89	0.87	B	CamW	···
HSC J0926+0500	141.6992	5.0005	0.49	0.462	2.68	1.88	0.64	B	RW	···
HSC J0935+0047	143.8137	0.7959	0.37	0.358	7.82	2.38	0.92	B	CamR	···
HSC J0943−0154	145.8653	−1.9149	0.44	0.450	2.42	1.56	0.50	B	Cam	···
HSC J0943+0059	145.9510	0.9903	0.43	···	2.43	3.00	0.00	A	CamR	2
HSC J0947−0111†	146.8682	−1.1925	0.26	0.239	4.08	2.00	0.47	B	CamW	···
HSC J0951−0014	147.9171	−0.2391	0.37	0.421	14.13	1.63	0.52	B	CamRW	···
HSC J0958+0109	149.6311	1.1603	0.57	0.550	2.72	2.11	0.60	B	Cam	···
HSC J0959+0101	149.8211	1.0329	0.45	0.446	3.08	1.67	0.47	B	CamRW	···
HSC J0959+0219	149.9833	2.3169	0.97	···	2.74	2.56	0.50	A	Cam	7
HSC J1005−0100	151.3869	−1.0078	0.40	0.420	6.19	1.67	0.47	B	CamW	···
HSC J1005−0103	151.4756	−1.0660	1.05	···	3.97	1.56	0.68	B	Cam	···
HSC J1007−0123†	151.8009	−1.3879	0.93	···	2.19	1.56	0.83	B	···	···
HSC J1018−0121	154.6972	−1.3591	0.39	0.388	3.21	2.88	0.35	A	RW	2
HSC J1039−0216	159.7807	−2.2750	0.16	···	2.05	2.11	0.74	B	W	4
HSC J1139−0218	174.8726	−2.3071	0.79	···	3.52	2.78	0.42	A	W	···
HSC J1143−0047	175.7553	−0.7867	0.28	···	2.61	1.75	0.46	B	CamRW	···
HSC J1143−0144	175.8743	−1.7418	0.11	0.106	2.56	3.00	0.00	A	RW	4,12
HSC J1143+0013†	175.9262	0.2278	0.65	0.650	5.17	2.29	0.70	B	Cam	···
HSC J1144−0025	176.1623	−0.4299	0.73	0.614	2.23	2.00	0.76	B	CamW	···
HSC J1147+0119	176.7731	1.3192	0.63	0.636	3.88	1.86	0.83	B	···	···
HSC J1147−0013^{X}	176.9383	−0.2307	0.81	···	3.31	2.29	0.45	B	···	···
HSC J1152+0031	178.0592	0.5239	0.46	0.466	5.43	2.71	0.45	A	CamW	4,5
HSC J1153−0144	178.3794	−1.7363	0.11	···	24.60	2.13	0.00	B	CamRW	···
HSC J1155+0053	178.8366	0.8843	0.31	0.283	3.65	1.71	0.45	B	···	4
HSC J1156−0019	179.0414	−0.3257	0.27	0.260	4.61	1.57	0.50	B	CamR	···
HSC J1156−0021	179.0451	−0.3501	0.26	0.256	8.01	1.86	0.35	B	CamRW	···
HSC J1156−0101	179.0548	−1.0339	0.44	···	4.60	1.57	0.50	B	Cam	4
HSC J1156−0037^{X}	179.2234	−0.6316	0.92	···	3.86	1.71	1.03	B	Cam	···
HSC J1201+0126^{X}	180.2978	1.4433	0.62	···	6.77	2.29	0.45	B	Cam	4
HSC J1201+0025	180.4603	0.4222	0.88	···	1.86	1.67	0.71	B	Cam	···
HSC J1202+0039^{X}	180.7370	0.6584	0.70	0.689	4.18	2.29	0.45	B	Cam	···
HSC J1207−0103	181.9302	−1.0654	0.18	0.180	2.21	2.44	0.50	B	CamW	4
HSC J1208+0128	182.2052	1.4791	0.71	···	2.20	2.22	0.42	B	Cam	···
HSC J1208−0103	182.2306	−1.0512	0.71	0.662	4.73	2.43	0.50	B	CamW	···
HSC J1210−0112	182.5947	−1.2001	0.59	0.574	4.05	2.14	0.35	B	Cam	4
HSC J1211+0020	182.9875	0.3482	0.79	···	2.72	1.56	0.50	B	Cam	···
HSC J1222−0127	185.6074	−1.4485	0.29	0.295	10.76	2.78	0.42	A	W	···
HSC J1223−0210	185.8964	−2.1754	0.35	0.439	4.39	1.89	0.57	B	RW	···
HSC J1224−0042	186.2094	−0.7044	0.40	0.403	2.41	2.56	0.50	A	CamR	4
HSC J1231+0023	187.7810	0.3921	0.60	0.591	5.94	1.89	0.87	B	CamW	···
HSC J1231+0301	187.8949	3.0313	0.42	0.461	6.18	1.78	0.63	B	W	···
HSC J1233−0144	188.2623	−1.7352	0.63	···	9.72	2.00	0.67	B	Cam	···
HSC J1233+0131	188.2803	1.5300	0.42	0.425	3.39	1.75	0.46	B	CamRW	4
HSC J1234+0007	188.6440	0.1190	1.04	···	2.13	1.78	0.63	B	Cam	···
HSC J1241+0347	190.4916	3.7893	0.34	0.414	3.37	1.63	0.52	B	R	···
HSC J1244+0413	191.2226	4.2208	0.33	0.322	4.66	2.75	0.46	A	RW	···
HSC J1249−0118	192.3172	−1.3085	0.48	···	9.11	1.56	0.83	B	W	···
HSC J1253+0437	193.4192	4.6181	0.22	0.243	4.60	3.00	0.00	A	W	···
HSC J1255+0102	193.8525	1.0358	0.34	0.374	10.38	1.63	0.52	B	RW	···
HSC J1308−0047	197.1898	−0.7886	0.18	0.188	11.22	2.33	0.47	B	W	···
HSC J1311−0120	197.8737	−1.3410	0.14	0.174	47.99	2.63	0.74	A	RW	17
HSC J1327+4305	201.8703	43.0833	0.36	0.374	10.78	2.75	0.46	A	RW	···
HSC J1337+0112	204.2834	1.2176	0.32	0.327	4.39	2.25	0.71	B	RW	4
HSC J1340+4410	205.1241	44.1676	0.44	0.546	5.96	2.33	0.47	B	···	···
HSC J1343+4155	205.8869	41.9175	0.40	0.418	12.83	3.00	0.00	A	RW	10
HSC J1349−0019†	207.2637	−0.3298	0.55	···	2.91	1.56	0.68	B	W	···
HSC J1400+0024	210.0880	0.4055	0.37	···	2.28	1.86	0.64	B	CamRW	···
HSC J1407−0028	211.9735	−0.4715	0.49	0.471	10.32	2.29	0.70	B	CamR	···
HSC J1410+0129	212.5043	1.4991	0.56	0.541	2.23	2.00	0.00	B	···	4,6
HSC J1410−0109	212.7087	−1.1607	0.65	···	2.03	1.67	0.50	B	Cam	···

Table 3. *Continued.*

Name	α(J2000)	δ(J2000)	$z_{\ell,\mathrm{phot}}$	$z_{\ell,\mathrm{spec}}$	R_{arc} (arcsec)	Rank	σ_{Rank}	Grade	PC	References
HSC J1411+0107	212.9073	1.1223	0.48	0.462	2.57	2.29	0.70	B	CAMW	4
HSC J1414−0136	213.5874	−1.6128	0.53	0.511	5.52	3.00	0.00	A	···	···
HSC J1418+0044	214.5233	0.7431	0.92	···	3.53	1.71	1.03	B	CAM	···
HSC J1419+0020†	214.7852	0.3469	0.36	0.339	4.25	2.29	0.70	B	···	···
HSC J1420+0057	215.0694	0.9547	0.49	0.507	10.96	2.29	0.70	B	RW	···
HSC J1420+0058	215.0743	0.9755	0.34	0.330	3.24	2.29	0.45	B	CAMW	4
HSC J1420+0007	215.2019	0.1258	0.58	0.545	3.67	2.29	0.70	B	CAM	···
HSC J1421+0022	215.2655	0.3720	0.67	···	2.29	2.29	0.45	B	CAM	2
HSC J1421−0024	215.4578	−0.4009	0.62	···	3.15	1.56	0.50	B	CAM	···
HSC J1423−0026†	215.9747	−0.4345	0.59	0.636	14.29	2.43	0.50	B	CAM	···
HSC J1424−0053	216.2042	−0.8892	0.87	0.795	3.33	2.86	0.35	A	CAM	4,5,11
HSC J1424+0042	216.2077	0.7004	0.47	0.477	5.29	1.57	0.50	B	CAMW	···
HSC J1427+0043	216.7776	0.7207	0.28	0.295	2.63	2.00	0.76	B	CAMW	4
HSC J1428+0043	217.0751	0.7252	0.32	0.335	8.48	1.57	0.50	B	CAMRW	···
HSC J1431−0006	217.8081	−0.1037	0.70	···	2.45	2.14	0.35	B	CAM	···
HSC J1434+4315	218.6586	43.2615	0.38	0.385	2.11	2.25	0.89	B	RW	···
HSC J1434−0056	218.7267	−0.9496	0.76	0.728	2.74	2.57	0.73	A	CAM	5
HSC J1435−0106	218.8296	−1.1101	0.78	···	2.69	1.78	0.67	B	CAM	···
HSC J1436+4329	219.0464	43.4891	0.39	0.386	2.70	3.00	0.00	A	W	···
HSC J1437−0002	219.3929	−0.0488	0.63	0.627	3.62	2.29	0.45	B	CAM	···
HSC J1441−0018	220.3623	−0.3164	0.35	0.287	5.32	2.29	0.45	B	···	···
HSC J1441−0053	220.3862	−0.8996	0.57	···	8.93	3.00	0.00	A	CAMW	···
HSC J1443+0102†	220.7898	1.0362	0.59	0.529	13.19	1.86	0.83	B	CAMW	···
HSC J1444−0051	221.1198	−0.8617	0.53	0.575	2.04	2.29	0.88	B	···	4,5
HSC J1449−0002	222.4072	−0.0452	0.57	0.529	2.97	1.71	0.70	B	CAM	···
HSC J1450+0055	222.6666	0.9279	0.44	0.421	9.95	2.86	0.35	A	···	···
HSC J1451+0111	222.7769	1.1927	0.37	0.391	2.12	1.57	0.50	B	···	4
HSC J1458−0024	224.6513	−0.4000	0.65	0.595	3.93	2.29	0.45	B	CAMW	4
HSC J1459+4410	224.8790	44.1802	0.32	0.323	3.03	1.57	0.35	B	CAMRW	···
HSC J1459−0055	224.9882	−0.9230	0.60	0.939	2.22	1.56	0.68	B	CAMW	···
HSC J1507+4244	226.8466	42.7340	0.23	0.218	11.15	1.75	0.71	B	CAMRW	···
HSC J1508+4256	227.1544	42.9415	0.80	···	8.82	1.89	0.31	B	CAM	···
HSC J1510+4255	227.6903	42.9324	0.75	···	7.38	2.22	0.63	B	CAM	···
HSC J1513+4333	228.4882	43.5582	0.24	0.237	2.45	1.63	0.52	B	CAMRW	···
HSC J1522+4235	230.6975	42.5944	0.39	0.379	4.74	1.63	0.52	B	CAMRW	···
HSC J1525+4227	231.2877	42.4642	0.85	···	2.28	2.22	0.63	B	···	···
HSC J1525+4409	231.4855	44.1613	0.39	0.388	3.05	1.89	0.31	B	CAMR	···
HSC J1526+4406	231.6363	44.1044	0.48	0.487	2.15	1.67	0.47	B	···	···
HSC J1557+4206	239.3841	42.1066	0.46	···	2.15	2.33	0.67	B	···	···
HSC J1559+4232	239.8367	42.5423	0.85	···	4.37	1.56	0.50	B	CAM	···
HSC J1602+4346†	240.5990	43.7726	0.42	···	2.30	1.86	0.64	B	CAM	···
HSC J1602+4346	240.6045	43.7709	0.42	···	3.38	2.29	0.45	B	CAM	···
HSC J1602+4335	240.7110	43.5849	0.41	0.414	4.56	2.43	0.50	B	CAMRW	···
HSC J1602+4335	240.7214	43.5837	0.45	···	2.81	2.00	0.00	B	CAMRW	···
HSC J1618+4345	244.5774	43.7574	0.72	0.899	4.69	2.11	0.78	B	···	···
HSC J1618+5430	244.5857	54.5052	0.79	···	2.10	2.56	0.73	A	CAM	···
HSC J1620+4318	245.1101	43.3104	0.71	···	3.99	2.29	0.70	B	···	···
HSC J1621+4245	245.3623	42.7616	0.13	0.138	13.00	1.71	0.70	B	CAMRW	···
HSC J1629+4349	247.4261	43.8280	0.55	0.528	6.33	1.71	0.70	B	CAMRW	···
HSC J1631+4234†	247.7866	42.5781	0.68	···	2.12	1.57	0.90	B	CAM	···
HSC J1632+4246†	248.2406	42.7699	0.22	0.228	2.20	3.00	0.00	A	W	16
HSC J2202+0234	330.7369	2.5761	0.49	0.482	6.60	2.29	0.70	B	CAMFRW	8
HSC J2203+0426	330.9438	4.4459	0.51	0.527	8.28	2.00	0.67	B	F	···
HSC J2205+0147	331.2789	1.7844	0.48	0.476	2.36	1.67	0.82	B	F	7
HSC J2205+0210†	331.3976	2.1760	0.26	0.252	3.29	1.56	0.68	B	W	···
HSC J2206+0411	331.6751	4.1919	0.53	0.537	4.24	1.56	0.68	B	FW	7
HSC J2207+0224†	331.8298	2.4046	0.42	0.418	3.50	2.29	0.70	B	CAMF	···
HSC J2208+0206	332.2499	2.1152	1.04	···	5.83	2.57	0.73	A	CAMF	···
HSC J2209−0034	332.4829	−0.5764	0.69	0.716	4.06	2.00	0.93	B	CAMF	···
HSC J2212−0008	333.0476	−0.1389	0.36	0.365	3.40	2.29	0.70	B	CAMFRW	1
HSC J2212+0650	333.1505	6.8415	0.38	0.399	2.04	2.00	0.00	B	RW	···
HSC J2213−0018	333.2770	−0.3084	0.40	0.408	7.60	1.57	0.50	B	CAMFRW	1
HSC J2213−0030	333.2789	−0.5103	0.64	0.702	2.75	1.57	0.90	B	CAMF	7
HSC J2213+0354†	333.3342	3.9100	0.69	0.670	5.01	2.44	0.50	B	CAM	···

Table 3. *Continued.*

Name	α(J2000)	δ(J2000)	$z_{\ell,\mathrm{phot}}$	$z_{\ell,\mathrm{spec}}$	R_{arc} (arcsec)	Rank	σ_{Rank}	Grade	PC	References
HSC J2213+0048[X]	333.3826	0.8100	0.95	···	5.19	2.29	0.45	B	F	7
HSC J2213+0056	333.4550	0.9475	0.28	···	3.14	1.57	0.50	B	CAM	···
HSC J2214+0110	333.5787	1.1772	0.63	0.566	3.57	1.57	0.90	B	CAMFW	1,7
HSC J2215+0102	333.8056	1.0446	0.71	···	2.26	1.89	0.60	B	CAMF	1
HSC J2215+0435	333.9658	4.5838	0.65	···	9.39	2.22	0.63	B	CAMW	···
HSC J2217−0038	334.3723	−0.6436	0.30	···	2.06	1.56	0.50	B	···	···
HSC J2221−0053	335.4324	−0.8842	0.34	0.334	4.98	1.78	0.42	B	CAM	···
HSC J2226+0041[X]	336.5386	0.6949	0.63	0.647	2.98	3.00	0.00	A	···	1,3,5
HSC J2226−0034	336.6597	−0.5805	0.38	0.404	2.20	1.78	0.42	B	CAMR	···
HSC J2228+0022	337.1687	0.3704	0.59	···	1.21	2.00	0.54	B	···	···
HSC J2230−0018†	337.5731	−0.3125	0.40	0.406	7.05	1.57	1.05	B	CAMR	···
HSC J2232+0057	338.0466	0.9501	0.40	0.401	2.38	1.71	0.45	B	CAMW	···
HSC J2232−0025	338.1611	−0.4261	1.08	···	2.13	3.00	0.00	A	CAM	···
HSC J2233−0104[X]	338.3201	−1.0694	0.95	···	22.15	1.57	1.05	B	···	···
HSC J2233−0019	338.3331	−0.3264	0.45	0.398	4.13	1.57	0.73	B	CAMR	···
HSC J2233+0157	338.4742	1.9560	0.27	···	2.08	2.22	0.63	B	CAMR	···
HSC J2235−0135	338.8841	−1.5944	0.48	···	3.05	1.56	0.96	B	W	···
HSC J2235+0003	338.9535	0.0509	0.76	0.735	8.66	1.71	0.70	B	CAM	···
HSC J2236+0616	339.0586	6.2723	0.37	0.350	3.40	2.13	0.64	B	W	···
HSC J2239+0235	339.8946	2.5853	1.13	···	1.91	3.00	0.00	A	CAM	···
HSC J2242+0011	340.5899	0.1956	0.39	0.385	2.43	3.00	0.00	A	CAMR	5
HSC J2243−0004	340.9990	−0.0803	0.71	0.690	3.31	1.71	0.00	B	···	···
HSC J2246+0558†	341.5610	5.9748	0.31	0.340	2.66	2.63	0.74	A	RW	···
HSC J2246+0415	341.6871	4.2637	1.02	···	8.67	2.33	0.47	B	CAM	···
HSC J2248+0147	342.2457	1.7865	0.38	0.360	6.74	2.00	0.00	B	CAMRW	5
HSC J2258+0031	344.5655	0.5248	0.26	0.256	4.80	1.75	0.46	B	CAMRW	···
HSC J2306+0225	346.7428	2.4286	0.35	0.362	3.17	2.00	0.00	B	CAMRW	6
HSC J2313−0104	348.4770	−1.0802	0.53	0.531	8.13	2.63	0.52	A	···	1,15
HSC J2314−0003	348.5673	−0.0529	0.60	···	2.64	1.56	0.68	B	W	···
HSC J2315+0129	348.9799	1.4850	0.46	0.424	3.68	1.56	0.83	B	CAMRW	6
HSC J2319+0038	349.9726	0.6369	0.94	···	7.69	2.33	0.82	B	CAM	···
HSC J2328+0005	352.2238	0.0937	0.50	0.443	3.67	2.00	0.00	B	CAM	···
HSC J2329−0120	352.4494	−1.3466	0.53	0.537	10.50	1.67	0.94	B	CAMW	1,15
HSC J2330+0133	352.5252	1.5512	0.42	0.444	3.44	1.67	0.67	B	CAMW	···
HSC J2330+0158	352.6815	1.9702	0.69	···	2.16	1.67	0.82	B	CAM	···
HSC J2332−0003	353.1491	−0.0511	0.52	0.510	3.76	1.71	0.45	B	CAMR	···
HSC J2337+0016	354.4175	0.2781	0.32	0.272	2.00	3.00	0.00	A	R	···
HSC J2346−0010	356.5148	−0.1829	0.26	0.261	2.30	1.56	0.68	B	RW	···
HSC J2351+0037	357.8388	0.6169	0.26	0.277	2.96	2.63	0.52	A	CAMRW	···
HSC J2352+0006	358.0488	0.1041	0.67	···	1.61	1.56	0.68	B	···	···
HSC J2359+0208	359.8898	2.1399	0.44	0.430	8.67	2.88	0.35	A	CAMRW	2

acquired through three arms, the ultraviolet (UVB, $\lambda\lambda$3,000 - 5,500 Å), the visual (VIS, $\lambda\lambda$5,000 - 10,500 Å), and the near-infrared (NIR, $\lambda\lambda$10,000 - 25,000 Å). The lensed sources were observed using slit widths of 1.0″, 0.9″, and 0.9″ in the UVB, VIS, and NIR arms, respectively, with a binning of 2×2 applied to the UVB and VIS data. We set the position angle (PA) of the long slit to be preferentially along the lensed arc (see Figure 6). In order to optimise sky background subtraction, we dithered the observations in the standard ABBA nodding pattern.

Each system was observed in slit mode during either one (e.g., HSC J0224−0336) or two (e.g., HSC J1202+0039) observation blocks (OBs), to reach the optimal signal to noise (S/N) ratio. Each OB corresponds to roughly one hour of telescope time, and consists of 10×285s exposures obtained in an ABBA nodding pattern, to optimise background subtraction in the NIR arm. Exposure times in the UVB and VIS arms are slightly shorter due to the longer read-out time. Observations were executed with a seeing FWHM < 0.9″ on target position. Initially, we reduce the spectroscopic data using the ESO REFLEX software (version 2.9.0) combined with X-shooter pipeline recipes (v3.1.0) (Freudling et al. 2013; Modigliani et al. 2010). The pipeline recipes performs standard bias subtraction and flat-fielding of the raw spectra. Cosmic rays are removed using `LACosmic` (van Dokkum 2001). For each arm, we extract the orders and rectify them in wavelength space using a wavelength solution previously obtained from the calibration frames. The resulting rectified orders are then shifted, co-added, and flux calibrated to obtain the final two-dimensional (2D) spectrum. For further data processing and analysis, we use standard IRAF tools. We produce 1D spectra using an extraction aperture in all three arms and for all three images of the source (apertures are shown by red and blue dashed line on Figure 6).

5.1 Redshift measurement

We visually inspected all of the three arms of the X-shooter (2D and 1D) spectra in order to identify any emission and/or absorption lines arising from the lensed galaxies. We identified a set of emission lines that could be attributed to a common redshift. We fitted Gaussian profiles to each of those lines in order to determine their central

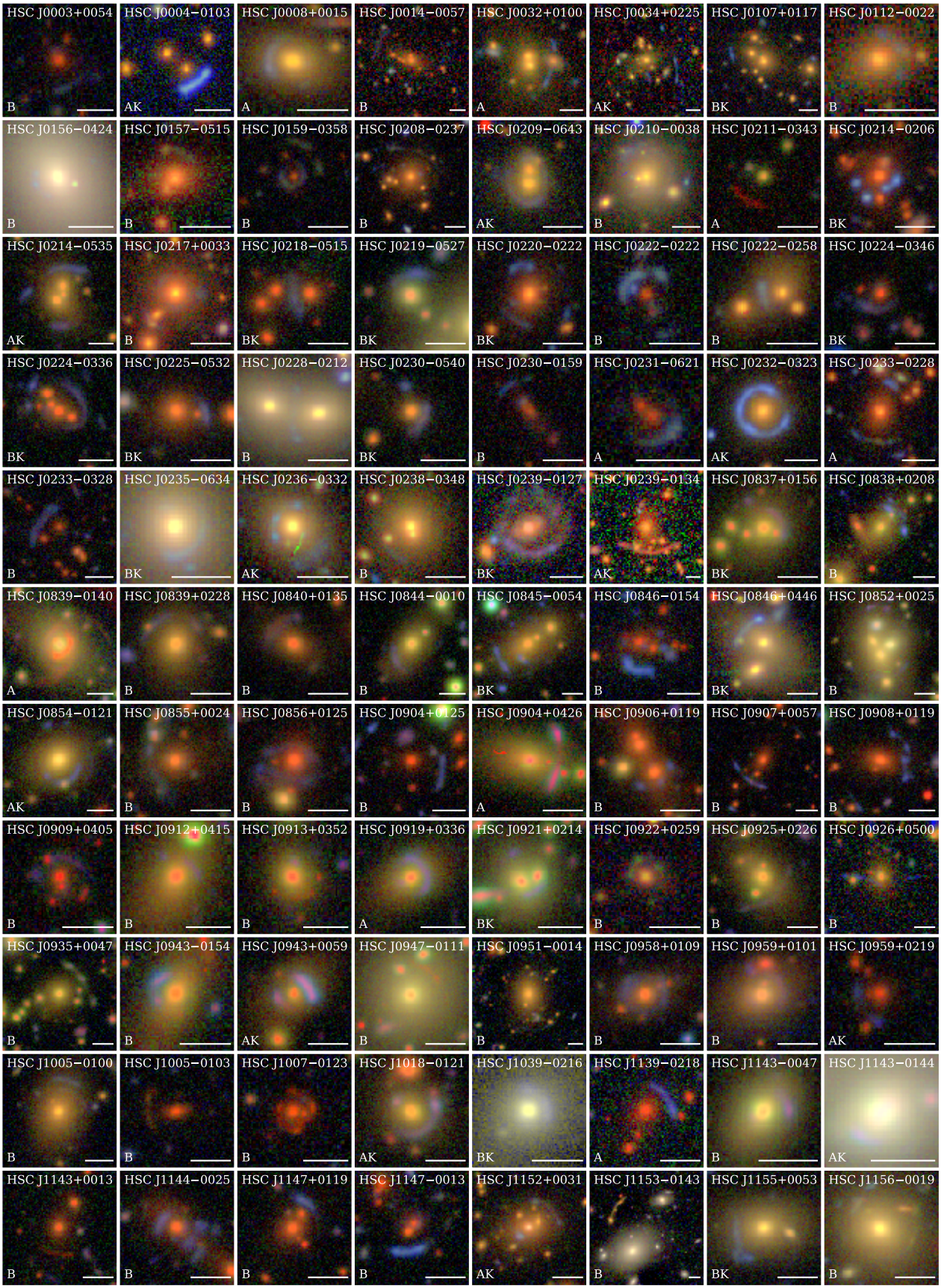

Figure 4. SuGOHI-c lens candidates with grades A and B (shown on the bottom left). Known lenses are indicated by "K". All images are oriented with North up and East left. A scale bars of 5″ are displayed in the bottom right corner.

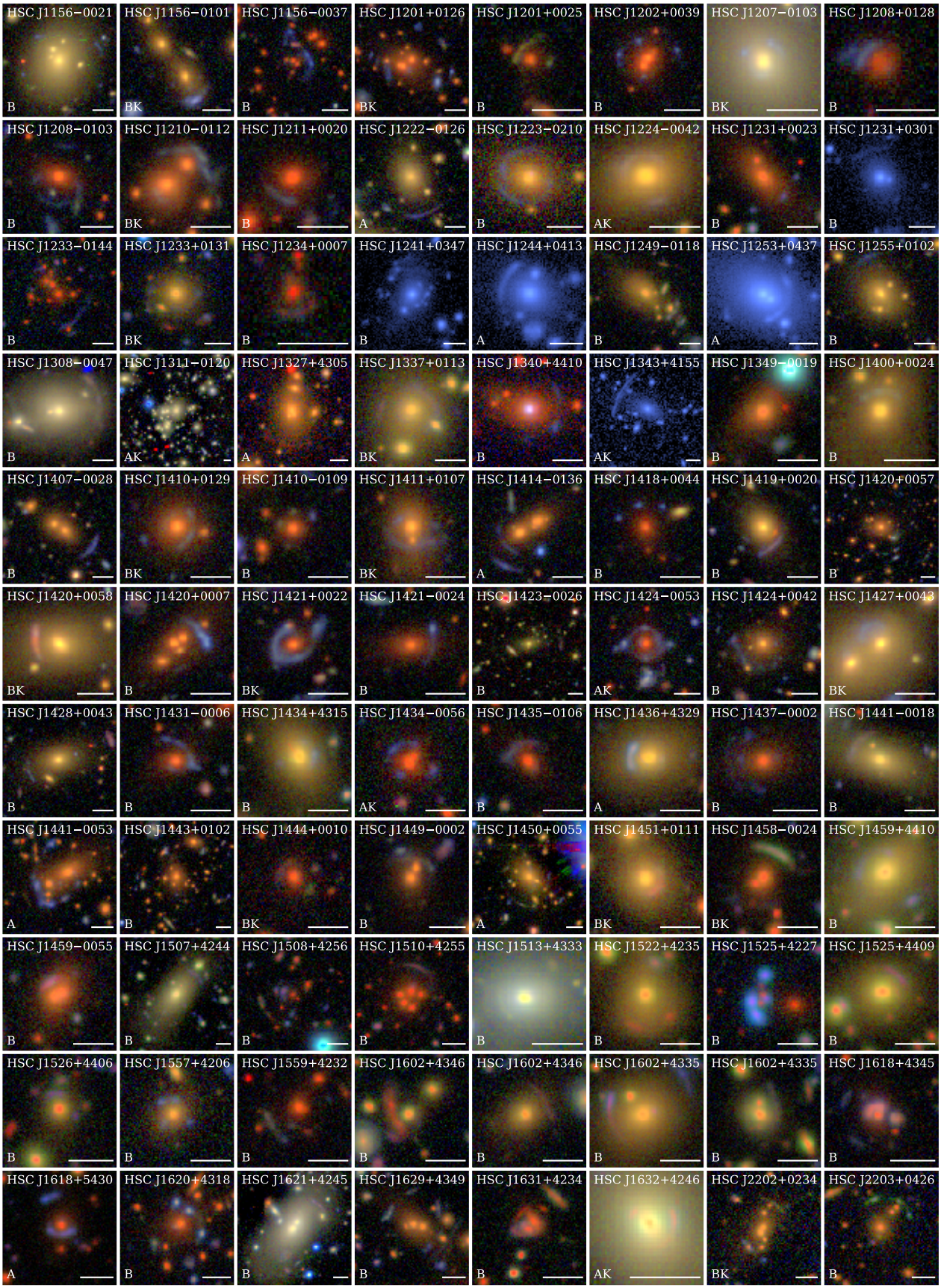

Figure 4. *Continued.*

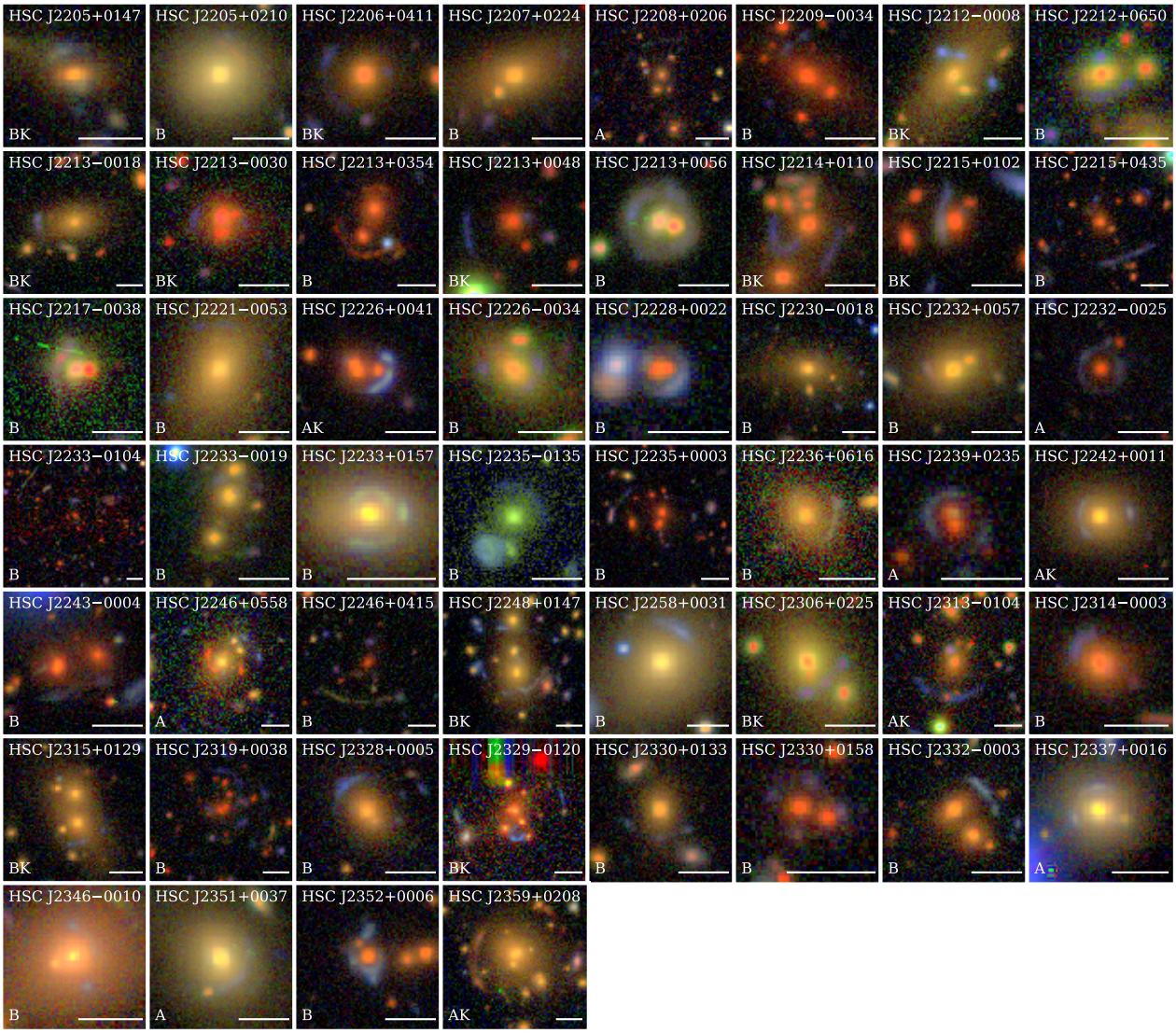

Figure 4. *Continued.*

Table 4. Summary of X-shooter spectroscopic observations. Position angles (P.A.) are measured East of North.

Name	Obs. Date (UT)	P.A. (deg)	z_s
HSC J0224−0336	13-07-2017	25	1.514
HSC J0904+0125	09-04-2017	5	2.176
HSC J0907+0057	29-01-2018	25	1.916
HSC J1147−0013	28-02-2018	102	2.093
HSC J1156−0037	07-04-2017	22	1.907
HSC J1201+0126	07-04-2017	7	1.653
HSC J1202+0039	06-04-2017 01-03-2018	−55	1.885
HSC J2213+0048	10-06-2017 15-08-2017	−18	...
HSC J2226+0041	29-09-2017	−50	1.897
HSC J2233−0104	07-08-2017	90	0.902

wavelength and, thereby, determined a mean redshift for each lensed galaxy. Most of the lensed arcs showed [OII] doublet λ3726.03, 3728.81 Å, Hδ λ4101.73 Å, Hγ λ4340.46 Å, Hβ λ4861.32 Å, [OIII] λ4958.91, 5006.84 Å, Hα λ6562.79 Å, [NII] λ6583.45 Å, [SII] λ6716.43, and λ6730.81 Å which are expected to be found in blue star forming galaxies. Our lensed galaxies span a redshift range from $z \sim 0.9$ to 2.2 (summarised in Table 4). We give a short description of the confirmed lenses below.

5.2 Spectroscopically confirmed group-scale lenses

HSC J0224−0336 at $z_{\ell,\mathrm{spec}} = 0.613$: This system has been reported in More et al. (2012) which has four bright early type galaxies at the centre, surrounded by a blue arc (almost complete ring). We set the slit along the arc to the North-West of the lens (see Figure 6) that has a peak flux in g-band. Most of the emission lines in this system are detected in the NIR arm of X-shooter, Hβ, [OIII], Hα, [NII] and [SII]. We also detected [OII] doublet in the VIS arm. These emission lines correspond to a mean redshift of $z = 1.514$. The lens galaxy, "G" of HSC J0224−0336 shown in Figure 6, is identified as the centre of the cluster by Wen et al. (2012) which has a richness of $N_{\mathrm{ric,WEN}} = 21.62$ with 14 member galaxies and corresponds to $M_{200} \approx 1.18 \times 10^{14} M_{\odot}$. However,

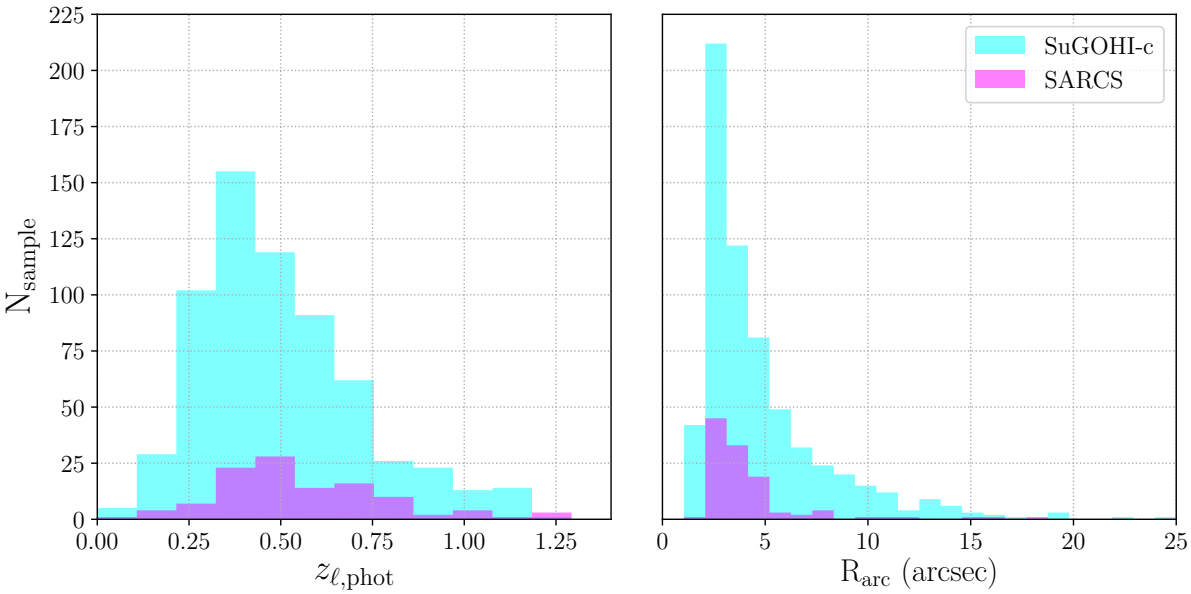

Figure 5. *Left:* Photometric redshift distributions of group-to-cluster-scale lens candidates. The peak of the redshift distributions for both the SuGOHI-c sample (cyan) and the SARCS sample (magenta, More et al. 2012) are around $z \sim 0.4$. *Right:* The binned distribution of arc radii for $R_{\rm arc} \geq 2$. The peak at around $3''$ attests to the fact that most of the candidates are, indeed, at group-scales, in our sample. As before, cyan and magenta show the SuGOHI-c and the SARCS samples, respectively.

the same galaxy is identified as a member galaxy of a cluster, in CAMIRA, with a richness of $N_{\rm ric,CAMIRA} = 19.62, 63$ member galaxies and $M_{200} \approx 6.36 \times 10^{13} M_\odot$. The stellar velocity dispersion of the lens galaxy is 448 ± 101 km s^{-1} from the SDSS data.

HSCJ0904+0125 at $z_{\ell,\rm phot} = 0.914$: For this system, we set the slit along a nearly north-south blue arc. We detected emission lines such as the [OII] doublet, Hβ, [OIII], and Hα in NIR arm which has a mean redshift of $z = 2.176$. The lens galaxy of the system, "G" in HSCJ0904+0125 panel of Figure 6, is identified as the galaxy member in CAMIRA. The cluster has a richness $N_{\rm ric,CAMIRA} = 18.37$ with 56 member galaxies and corresponds to $M_{200} \approx 5.83 \times 10^{13} M_\odot$.

HSC J0907+0057 at $z_{\ell,\rm phot} = 0.723$: This system is composed of a number of blue arcs around a bright early type galaxy at separation ($\simeq 5''$). We set a slit along the east-most arc-like component whose light is not contaminated by any red blobs (see Figure 4). We detect weak emission lines such as [OII] doublet and [OIII] λ5008.24 Å, yielding a lensed galaxy redshift of $z = 1.916$. The lens galaxy, "G" of HSC J0907+0057 shown in Figure 6, is at the centre of the cluster in CAMIRA which has a richness of $N_{\rm ric,CAMIRA} = 35.49$ and 75 member galaxies corresponding to $M_{200} \approx 1.38 \times 10^{14} M_\odot$.

HSC J1147−0013 at $z_{\ell,\rm phot} = 0.805$: We detect many strong emission lines such as [OII] doublet, Hγ, Hβ, [OIII] and Hα in the NIR arm from the almost straight blue arcs. This system has similar features with HSC J0904+0125 which has a small peak near main peak. We find that the emission lines has a mean redshift of $z = 2.093$. This group-scale system is found serendipitously during the inspection owing to the very bright arc and next to another cluster. The cluster catalogs may have missed this due to lack of sufficiently bright galaxies.

HSC J1156−0037 at $z_{\ell,\rm phot} = 0.918$: We find that the blue arc has a mean redshift of $z = 1.907$ from emission lines [OII] doublet, Hγ, Hβ, [OIII] and Hα in the NIR arm. The lens galaxy, "G" of HSC J1156−0037 shown in Figure 6, is found to be a galaxy member of the large cluster in CAMIRA which has a high richness of $N_{\rm ric,CAMIRA} = 64.05$ corresponding to $M_{200} \approx 3.00 \times 10^{14} M_\odot$. This cluster has 126 member galaxies.

HSC J1201+0126 at $z_{\ell,\rm phot} = 0.618$: This system has been reported in Petrillo et al. (2019). We set the slit along the blue arc which has a small early type galaxy included (which produces the continuum in the 2D spectra). We detect weak continuum from early type galaxy and strong emission lines, Hβ, [OIII] and Hα in NIR arm and [OII] doublet in VIS arm, yielding a lensed galaxy redshift of $z = 1.653$. The lens galaxy, "G" of HSC J1201+0126 shown in Figure 6, is at the centre of the cluster as per CAMIRA which has a richness of $N_{\rm ric,CAMIRA} = 36.23$ with 67 member galaxies and corresponds to $M_{200} \approx 1.42 \times 10^{14} M_\odot$.

HSC J1202+0039 at $z_{\ell,\rm spec} = 0.689$: As seen in Figure 6, the slit targeting this system covers the source in two locations, the East and North of the lens. We detect strong emission lines [OIII] λ4960.30 Å and [OIII] λ5008.24 Å in each source location. We find that the emission lines have a mean redshift of $z = 1.885$. The lens galaxy, "G" of HSC J1202+0039 shown in Figure 6, is identified as the BCG as per CAMIRA which has a richness of $N_{\rm ric,CAMIRA} = 36.298$ with 75 member galaxies and corresponding to $M_{200} \approx 1.42 \times 10^{14} M_\odot$. The stellar velocity dispersion of the BCG is 238 ± 37 km s^{-1} from the SDSS data.

HSC J2213+0048 at $z_{\ell,\rm phot} = 0.945$: We do not detect continuum and any features from emission or absorption in the spectrum of this system. The lens galaxy, "G" of HSC J2213+0048 shown in Figure 6, is identified to be a galaxy member in Ford et al. (2015) which has a richness of $N_{\rm ric,FORD} = 8.80$ with 68 member galaxies and corresponds to $M_{200} \approx 7.29 \times 10^{12} M_\odot$. This system also has been reported in More et al. (2012).

HSC J2226+0041 at $z_{\ell,\rm spec} = 0.647$: This is a known lens system (Diehl et al. 2017; Sonnenfeld et al. 2018; Jacobs et al. 2019). We measure a mean redshift of $z = 1.897$, from emission lines such

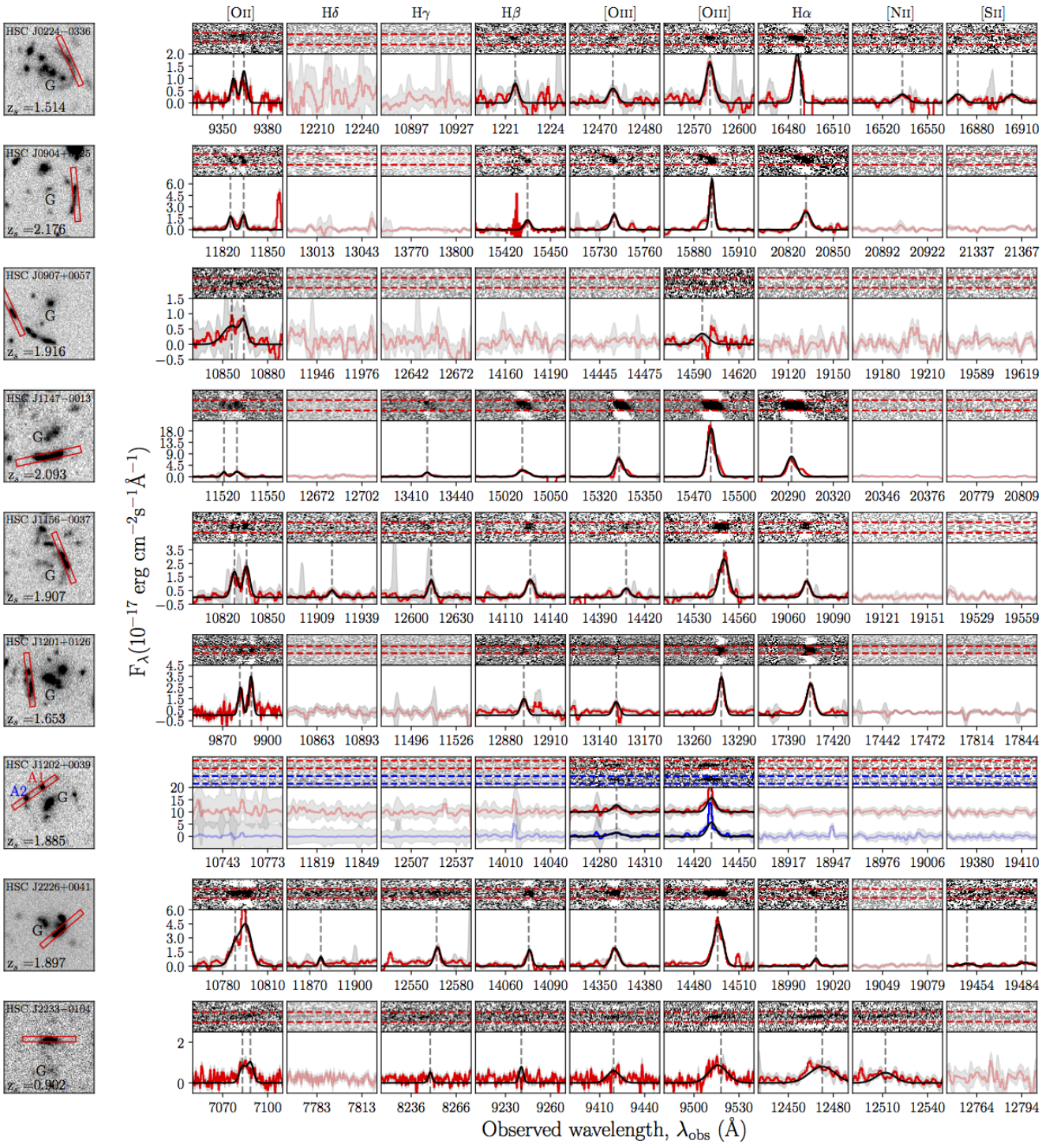

Figure 6. Spectroscopic results from the X-shooter observations. Each row is for one candidate lens. One candidate with no detection is not shown here. On the left, we show the alignment of the slit on the putative lensed source that was observed. The brightest lens galaxies are denoted by "G". On the right, the upper panel (for each row) shows regions from the 2D spectrum where interesting features are expected. The red (and blue) dashed lines show the exact region used for extracting the 1D spectrum of one of the lensed images (and its counterpart). The bottom panel shows the corresponding stacked 1D spectra (red) where the vertical lines highlight the location of expected emission lines. The labels for those emission lines are shown at the top of the figure. The error on the spectrum is shown by a shaded region (grey) and Gaussian fits to the emission lines are in black. The semi-transparent panels show the locations of some of the common emission lines, which are not detected, for the given source redshift.

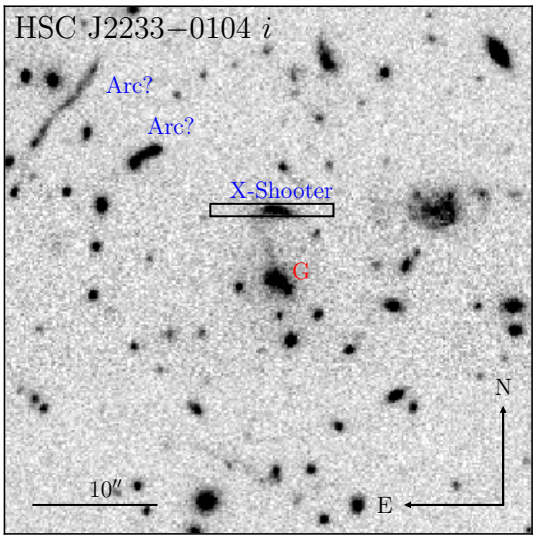

Figure 7. HSC J2233−0104 lens candidate. Image is ∼ 43″ on the side. The bar shows a scale of 10″.

as [OII] (assuming the rest-frame centroid of the unresolved [OII] doublet λ3728.3 Å), Hγ, Hβ, [OIII] λ4960.30 Å, [OIII] λ5008.24 Å, and Hα. The stellar velocity dispersion of the lens galaxy, "G" of HSC J2226+0041 shown in Figure 6, is 318 ± 47 km s^{-1} from the SDSS data.

HSC J2233−0104 at $z_{\ell,\mathrm{phot}} = 0.953$: We detect three probable blue arcs: a long-thin arc and a short arc to the North-East of the lens, and a third short arc to the North of the lens (see Figure 7). We set the slit along the northern arc and detect some emission lines, unresolved [OII] doublet λ3728.30, [OIII] λ4960.30 Å, [OIII] λ5008.24 Å, Hα, [NII] and also weak emission of Hβ. The emission lines suggest a mean redshift of $z = 0.902$, confirming the arc is probably not a lensed galaxy since the redshift of this arc is close to the photometric redshift of the lens galaxy, "G" of HSC J2233−0104 shown in Figure 6.

6 SUMMARY AND CONCLUSION

We have carried out the largest ever systematic search for strong gravitational lens systems at group-to-cluster-scales. Since the S18A release of the HSC-SSP Survey, covering nearly 1,114 deg^2, we have visually inspected 39,435 groups and clusters selected from four parent cluster catalogs. While CAMIRA catalog was obtained from HSC imaging, other catalogs (Wen et al. 2012; Ford et al. 2015; Rykoff et al. 2016) came from previous surveys with overlapping footprints.

Our search resulted in a total of 641 lens candidates with 228 highly promising (grade A-B) candidates and 413 plausible (grade C) candidates. Additionally, we report 131 galaxy-scale lens candidates found serendipitously during our search. Most of these are new and are missed from the previously reported SuGOHI-g samples (see Appendix A).

The SuGOHI-c will enable detailed studies of mass distributions in individual systems for even low-mass galaxy groups at low to intermediate redshifts and clusters at very high redshifts. Not to mention, the large sample size will surpass any of the previous statistical studies of group-scale lenses. Finally, we have nearly six times more lenses at high redshifts ($z_\ell > 0.8$) compared to the previous high-redshift SARCS sample. Thus, we will be able to study evolution in the mass distributions, at these mass scales, for the first time.

The SuGOHI-c sample has many striking systems with blue giant arcs, red lensed galaxies and in some cases, multiple lensed galaxies from distinct redshifts lensed by the same galaxy groups. We also present the results of our spectroscopic follow-up with X-shooter where, for 9 out of the 10 candidates, we could detect emission lines and successfully measure the redshifts of the lensed galaxies. A detailed mass modelling analysis using spectroscopic results will be presented in the near future.

ACKNOWLEDGEMENTS

ATJ and KTI are supported by JSPS KAKENHI Grant Number JP17H02868. MO is supported by JSPS KAKENHI Grant Number JP15H05892 and JP18K03693. IK is supported by JSPS KAKENHI Grant Number JP15H05896. SHS thanks the Max Planck Society for support through the Max Planck Research Group. J. H. H. C. acknowledges support from the Swiss National Science Foundation (SNSF). This work was supported in part by World Premier International Research centre Initiative (WPI Initiative), MEXT, Japan. The Hyper Suprime-Cam (HSC) collaboration includes the astronomical communities of Japan and Taiwan, and Princeton University. The HSC instrumentation and software were developed by the National Astronomical Observatory of Japan (NAOJ), the Kavli Institute for the Physics and Mathematics of the Universe (Kavli IPMU), the University of Tokyo, the High Energy Accelerator Research Organization (KEK), the Academia Sinica Institute for Astronomy and Astrophysics in Taiwan (ASIAA), and Princeton University. Funding was contributed by the FIRST program from Japanese Cabinet Office, the Ministry of Education, Culture, Sports, Science and Technology (MEXT), the Japan Society for the Promotion of Science (JSPS), Japan Science and Technology Agency (JST), the Toray Science Foundation, NAOJ, Kavli IPMU, KEK, ASIAA, and Princeton University.

This paper makes use of software developed for the Large Synoptic Survey Telescope. We thank the LSST Project for making their code available as free software at http://dm.lsst.org. The Pan-STARRS1 Surveys (PS1) have been made possible through contributions of the Institute for Astronomy, the University of Hawaii, the Pan-STARRS Project Office, the Max-Planck Society and its participating institutes, the Max Planck Institute for Astronomy, Heidelberg and the Max Planck Institute for Extraterrestrial Physics, Garching, The Johns Hopkins University, Durham University, the University of Edinburgh, Queen's University Belfast, the Harvard-Smithsonian centre for Astrophysics, the Las Cumbres Observatory Global Telescope Network Incorporated, the National Central University of Taiwan, the Space Telescope Science Institute, the National Aeronautics and Space Administration under Grant No. NNX08AR22G issued through the Planetary Science Division of the NASA Science Mission Directorate, the National Science Foundation under Grant No. AST-1238877, the University of Maryland, and Eotvos Lorand University (ELTE) and the Los Alamos National Laboratory.

Based [in part] on data collected at the Subaru Telescope and retrieved from the HSC data archive system, which is operated by Subaru Telescope and Astronomy Data centre at National Astronomical Observatory of Japan.

Funding for the Sloan Digital Sky Survey IV has been provided by the Alfred P. Sloan Foundation, the U.S. Department of

Energy Office of Science, and the Participating Institutions. SDSS acknowledges support and resources from the centre for High-Performance Computing at the University of Utah. The SDSS web site is www.sdss.org.

SDSS is managed by the Astrophysical Research Consortium for the Participating Institutions of the SDSS Collaboration including the Brazilian Participation Group, the Carnegie Institution for Science, Carnegie Mellon University, the Chilean Participation Group, the French Participation Group, Harvard-Smithsonian centre for Astrophysics, Instituto de Astrofísica de Canarias, The Johns Hopkins University, Kavli Institute for the Physics and Mathematics of the Universe (IPMU)/University of Tokyo, the Korean Participation Group, Lawrence Berkeley National Laboratory, Leibniz Institut für Astrophysik Potsdam (AIP), Max-Planck-Institut für Astronomie (MPIA Heidelberg), Max-Planck-Institut für Astrophysik (MPA Garching), Max-Planck-Institut für Extraterrestrische Physik (MPE), National Astronomical Observatories of China, New Mexico State University, New York University, University of Notre Dame, Observatório Nacional/MCTI, The Ohio State University, Pennsylvania State University, Shanghai Astronomical Observatory, United Kingdom Participation Group, Universidad Nacional Autónoma de México, University of Arizona, University of Colorado Boulder, University of Oxford, University of Portsmouth, University of Utah, University of Virginia, University of Washington, University of Wisconsin, Vanderbilt University, and Yale University.

REFERENCES

Aguado D. S., et al., 2019, ApJS, 240, 23
Aihara H., et al., 2018a, PASJ, 70, S4
Aihara H., et al., 2018b, PASJ, 70, S8
Aihara H., et al., 2019, PASJ, p. 106
Axelrod T., Kantor J., Lupton R. H., Pierfederici F., 2010, in Software and Cyberinfrastructure for Astronomy. p. 774015, doi:10.1117/12.857297
Balogh M. L., et al., 2009, MNRAS, 398, 754
Balogh M. L., et al., 2011, MNRAS, 412, 2303
Barnabè M., Czoske O., Koopmans L. V. E., Treu T., Bolton A. S., Gavazzi R., 2009, MNRAS, 399, 21
Bolton A. S., Burles S., Koopmans L. V. E., Treu T., Gavazzi R., Moustakas L. A., Wayth R., Schlegel D. J., 2008, ApJ, 682, 964
Bonvin V., et al., 2017, MNRAS, 465, 4914
Bosch J., et al., 2018, PASJ, 70, S5
Cabanac R. A., et al., 2007, A&A, 461, 813
Carrasco M., et al., 2017, ApJ, 834, 210
Chan J. H. H., et al., 2019, arXiv e-prints, p. arXiv:1911.02587
Coupon J., Czakon N., Bosch J., Komiyama Y., Medezinski E., Miyazaki S., Oguri M., 2018, PASJ, 70, S7
Dai X., Bregman J. N., Kochanek C. S., Rasia E., 2010, ApJ, 719, 119
Dark Energy Survey Collaboration et al., 2016, MNRAS, 460, 1270
Dey A., et al., 2019, AJ, 157, 168
Diehl H. T., et al., 2017, ApJS, 232, 15
Eisenstein D. J., et al., 2011, AJ, 142, 72
Faure C., et al., 2008, ApJS, 176, 19
Faure C., et al., 2011, A&A, 529, A72
Ferreras I., Saha P., Leier D., Courbin F., Falco E. E., 2010, MNRAS, 409, L30
Foëx G., Motta V., Limousin M., Verdugo T., More A., Cabanac R., Gavazzi R., Muñoz R. P., 2013, A&A, 559, A105
Foëx G., Motta V., Jullo E., Limousin M., Verdugo T., 2014, A&A, 572, A19
Ford J., Hildebrandt H., Van Waerbeke L., Erben T., Laigle C., Milkeraitis M., Morrison C. B., 2014, MNRAS, 439, 3755
Ford J., et al., 2015, MNRAS, 447, 1304
Freudling W., Romaniello M., Bramich D. M., Ballester P., Forchi V., García-Dabló C. E., Moehler S., Neeser M. J., 2013, A&A, 559, A96
Furusawa H., et al., 2018, PASJ, 70, S3
Gavazzi R., Treu T., Rhodes J. D., Koopmans L. V. E., Bolton A. S., Burles S., Massey R. J., Moustakas L. A., 2007, ApJ, 667, 176
Gladders M. D., Hoekstra H., Yee H. K. C., Hall P. B., Barrientos L. F., 2003, ApJ, 593, 48
Grillo C., 2010, ApJ, 722, 779
Hammer F., 1991, ApJ, 383, 66
Helsdon S. F., Ponman T. J., 2000, MNRAS, 315, 356
Heymans C., et al., 2012, MNRAS, 427, 146
Hezaveh Y. D., et al., 2016, ApJ, 823, 37
Hsieh B. C., Yee H. K. C., 2014, ApJ, 792, 102
Huang S., et al., 2018, PASJ, 70, S6
Huang X., et al., 2019, arXiv e-prints, p. arXiv:1906.00970
Ivezić Ž., et al., 2008, Serbian Astronomical Journal, 176, 1
Ivezić Ž., et al., 2019, ApJ, 873, 111
Jacobs C., et al., 2019, ApJS, 243, 17
Jaelani A. T., et al., 2019, arXiv e-prints, p. arXiv:1909.00120
Jurić M., et al., 2017, in Lorente N. P. F., Shortridge K., Wayth R., eds, Astronomical Society of the Pacific Conference Series Vol. 512, Astronomical Data Analysis Software and Systems XXV. p. 279 (arXiv:1512.07914)
Kawanomoto S., et al., 2018, PASJ, 70, 66
Komiyama Y., et al., 2018, PASJ, 70, S2
Koopmans L. V. E., Treu T., 2003, ApJ, 583, 606
Koopmans L. V. E., Treu T., Bolton A. S., Burles S., Moustakas L. A., 2006, ApJ, 649, 599
Koopmans L. V. E., et al., 2009, in astro2010: The Astronomy and Astrophysics Decadal Survey. (arXiv:0902.3186)
Krusch E., Rosenbaum D., Dettmar R. J., Bomans D. J., Taylor C. L., Aronica G., Elwert T., 2006, A&A, 459, 759
Limousin M., et al., 2009, A&A, 502, 445
Mandelbaum R., Seljak U., Hirata C. M., 2008, J. Cosmology Astropart. Phys., 8, 006
Marshall P. J., et al., 2016, MNRAS, 455, 1171
Milkeraitis M., van Waerbeke L., Heymans C., Hildebrand t H., Dietrich J. P., Erben T., 2010, MNRAS, 406, 673
Miyazaki S., et al., 2018, PASJ, 70, S1
Modigliani A., et al., 2010, in Silva D. R., Peck A. B., Soifer B. T., eds, Vol. 7737, Observatory Operations: Strategies, Processes, and Systems III. SPIE, pp 572 – 583, doi:10.1117/12.857211, https://doi.org/10.1117/12.857211
More A., McKean J. P., Muxlow T. W. B., Porcas R. W., Fassnacht C. D., Koopmans L. V. E., 2008, MNRAS, 384, 1701
More A., McKean J. P., More S., Porcas R. W., Koopmans L. V. E., Garrett M. A., 2009, MNRAS, 394, 174
More A., Jahnke K., More S., Gallazzi A., Bell E. F., Barden M., Häußler B., 2011, ApJ, 734, 69
More A., Cabanac R., More S., Alard C., Limousin M., Kneib J. P., Gavazzi R., Motta V., 2012, ApJ, 749, 38
More A., et al., 2016, MNRAS, 455, 1191
Murata R., et al., 2019, PASJ, 71, 107
Newman A. B., Ellis R. S., Treu T., 2015, ApJ, 814, 26
Oguri M., 2006, MNRAS, 367, 1241
Oguri M., 2014, MNRAS, 444, 147
Oguri M., Bayliss M. B., Dahle H., Sharon K., Gladders M. D., Natarajan P., Hennawi J. F., Koester B. P., 2012, MNRAS, 420, 3213
Oguri M., et al., 2018, PASJ, 70, S20
Parker L. C., Hudson M. J., Carlberg R. G., Hoekstra H., 2005, ApJ, 634, 806
Petrillo C. E., et al., 2019, MNRAS, 484, 3879
Richard J., Jones T., Ellis R., Stark D. P., Livermore R., Swinbank M., 2011, MNRAS, 413, 643
Rines K., Diaferio A., 2010, AJ, 139, 580
Ruff A. J., Gavazzi R., Marshall P. J., Treu T., Auger M. W., Brault F., 2011, ApJ, 727, 96
Rykoff E. S., et al., 2014, ApJ, 785, 104

Table A1. Lens candidate statistics for SuGOHI-g, similar with Table 2.

	Grade			Total	Known
	A	B	C		
SuGOHI-g	6	35	90	131	15
CAM	1	5	32	38	3
F	2	4	13	19	7
R	0	5	11	16	3
W	0	8	14	22	4
Serendipity	4	20	38	62	3

Rykoff E. S., et al., 2016, ApJS, 224, 1
Sonnenfeld A., Treu T., Gavazzi R., Marshall P. J., Auger M. W., Suyu S. H., Koopmans L. V. E., Bolton A. S., 2012, ApJ, 752, 163
Sonnenfeld A., et al., 2018, PASJ, 70, S29
Sonnenfeld A., Jaelani A. T., Chan J., More A., Suyu S. H., Wong K. C., Oguri M., Lee C.-H., 2019, A&A, 630, A71
Stark D. P., et al., 2013, MNRAS, 436, 1040
Suyu S. H., Marshall P. J., Auger M. W., Hilbert S., Blandford R. D., Koopmans L. V. E., Fassnacht C. D., Treu T., 2010, ApJ, 711, 201
Swinbank A. M., et al., 2009, MNRAS, 400, 1121
Tanaka M., et al., 2016, ApJ, 826, L19
Tanaka M., et al., 2018, PASJ, 70, S9
Treu T., Auger M. W., Koopmans L. V. E., Gavazzi R., Marshall P. J., Bolton A. S., 2010, ApJ, 709, 1195
Tyson J. A., Valdes F., Wenk R. A., 1990, ApJ, 349, L1
Vegetti S., Czoske O., Koopmans L. V. E., 2010a, MNRAS, 407, 225
Vegetti S., Koopmans L. V. E., Bolton A., Treu T., Gavazzi R., 2010b, MNRAS, 408, 1969
Verdugo T., et al., 2014, A&A, 571, A65
Vernet J., et al., 2011, A&A, 536, A105
Wen Z. L., Han J. L., Liu F. S., 2012, ApJS, 199, 34
Wong K. C., et al., 2018, ApJ, 867, 107
Wong K. C., et al., 2019, arXiv e-prints, p. arXiv:1907.04869
York D. G., et al., 2000, AJ, 120, 1579
Zitrin A., Broadhurst T., 2009, ApJ, 703, L132
de Jong J. T. A., et al., 2015, A&A, 582, A62
van Dokkum P. G., 2001, PASP, 113, 1420

APPENDIX A: ADDITIONAL SERENDIPITOUS LENS CANDIDATES FROM THE HSC-SSP S18A

During our visual inspection of galaxy groups and clusters, some galaxy-scale lenses were discovered serendipitously which happen to be either the member galaxies of the group or field galaxies in the vicinity. Since the lensing is due to an individual galaxy rather than a group/cluster (e.g., see the right most panel of Figure 2), these systems are excluded from our formal SuGOHI-c sample and are reported here instead.

This paper has been typeset from a TEX/LATEX file prepared by the author.

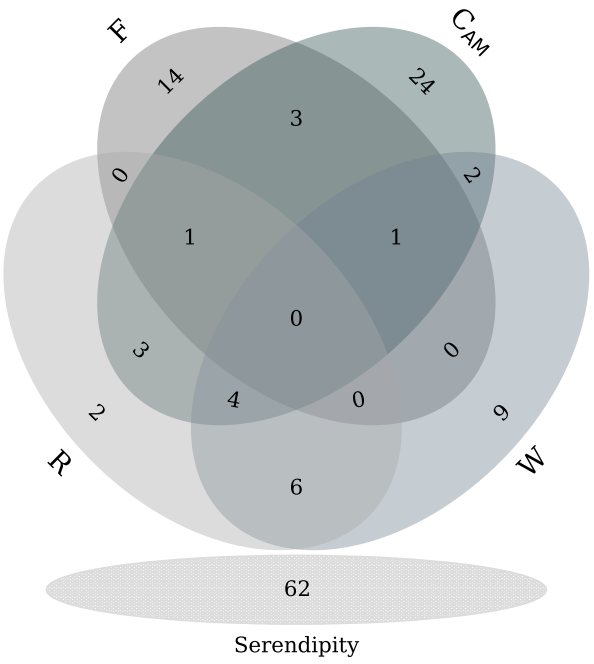

Figure A1. Similar with Figure 3, distribution of lens candidates at galaxy-scale according to the parent cluster catalogs with $R_{arc} < 2''$. The Venn diagram is divided into two panels: 69 lens systems of SuGOHI-g correspond to the parent cluster (upper) and 62 lens systems which serendipiously (bottom) discovered during the inspection.

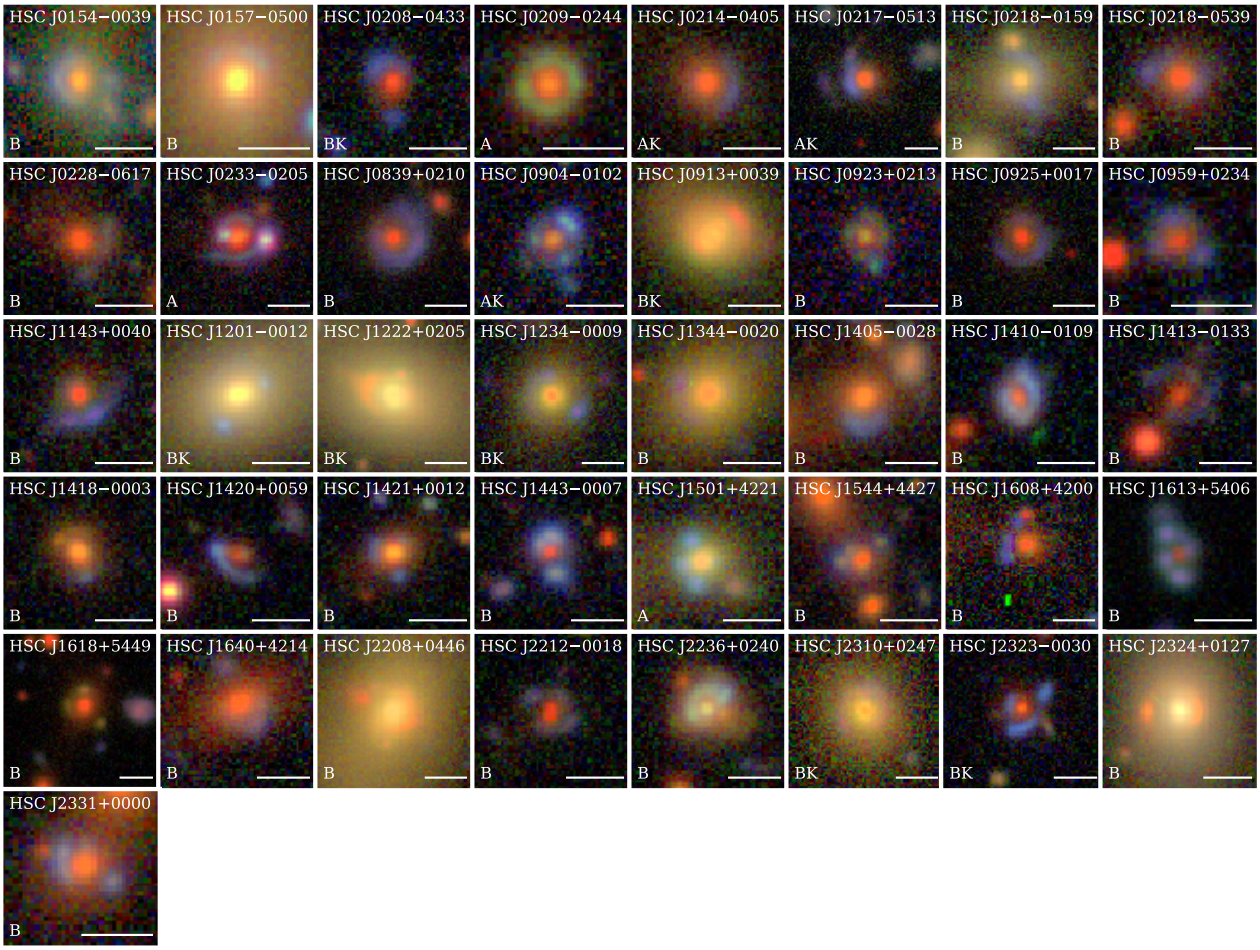

Figure A2. Lens candidates at galaxy-scale with grades A and B (labels shown on the bottom left). Known lenses are indicated by "K". All images are oriented with North up and East left. A scale bars 3″are displayed in the bottom right corner. The grade C from this sample are made available on the same page as the formal SuGOHI-c sample (http://www-utap.phys.s.u-tokyo.ac.jp/~oguri/sugohi/).

Table A2. Extra lens candidates at galaxy-scales discovered serendipitously. References: [3]Jacobs et al. (2019), [4]Petrillo et al. (2019), [5]Sonnenfeld et al. (2018), [6]Wong et al. (2018), [7]More et al. (2012), [8]More et al. (2016), [9]Cabanac et al. (2007), [18]Jaelani et al. (2019).

Name	α(J2000)	δ(J2000)	$z_{\ell,\mathrm{phot}}$	$z_{\ell,\mathrm{spec}}$	R_{arc} (arcsec)	Rank	σ_{Rank}	Grade	PC	References
HSC J0154−0039	28.6032	−0.6610	0.18	···	1.31	1.89	0.74	B	···	···
HSC J0157−0500	29.3327	−5.0109	0.28	···	1.32	2.22	0.42	B	CAMRW	···
HSC J0208−0433	32.1339	−4.5544	0.75	···	1.46	1.89	0.60	B	F	8
HSC J0209−0244	32.4809	−2.7451	0.56	···	1.10	3.00	0.00	A	···	···
HSC J0214−0405	33.5467	−4.0842	0.65	0.609	1.90	3.00	0.00	A	F	7,9
HSC J0217−0513	34.4048	−5.2249	0.64	0.646	1.71	3.00	0.00	A	CAMF	3,9
HSC J0218−0159	34.5994	−1.9844	0.28	···	1.82	1.75	0.71	B	CAMW	···
HSC J0218−0539	34.5983	−5.6558	0.67	0.691	1.92	1.56	0.68	B	F	···
HSC J0228−0617	37.1722	−6.2915	0.73	···	1.87	1.57	0.50	B	CAMF	···
HSC J0233−0205	38.3446	−2.0920	0.49	···	1.68	2.71	0.45	A	···	···
HSC J0839+0210	129.8766	2.1733	0.67	···	1.91	1.56	0.68	B	···	···
HSC J0904−0102	136.1239	−1.0412	0.82	0.957	1.33	3.00	0.00	A	···	18
HSC J0913+0039†	138.3797	0.6516	0.37	0.409	1.73	1.56	0.96	B	···	4,5
HSC J0923+0213	140.7907	2.2308	1.05	···	1.10	2.00	0.50	B	···	···
HSC J0925+0017	141.4375	0.2841	0.85	···	1.81	2.22	0.67	B	···	···
HSC J0959+0234	149.8789	2.5743	1.13	···	1.01	1.78	0.63	B	···	···
HSC J1143+0040	175.8242	0.6760	0.36	···	1.71	1.67	0.47	B	···	···
HSC J1201−0012	180.4162	−0.2073	0.25	···	1.89	1.56	0.50	B	R	4
HSC J1222+0205†	185.6720	2.0995	0.24	0.229	1.85	1.75	0.71	B	RW	4
HSC J1234−0009	188.5910	−0.1573	0.41	···	1.69	1.89	0.31	B	CAM	4
HSC J1344−0020	206.2318	−0.3376	0.42	···	1.76	1.56	0.50	B	···	···
HSC J1405−0028	211.2849	−0.4751	0.56	···	1.78	1.63	0.52	B	RW	···
HSC J1410−0109	212.7040	−1.1630	0.66	···	1.07	2.44	0.73	B	···	···
HSC J1413−0133	213.4980	−1.5600	0.96	···	1.51	1.56	0.68	B	···	···
HSC J1418−0003	214.7199	−0.0660	0.55	···	1.46	1.89	0.60	B	···	···
HSC J1420+0059	215.0560	0.9905	0.96	···	1.45	1.78	0.67	B	···	···
HSC J1421+0012	215.3635	0.2015	0.55	···	1.30	1.89	0.57	B	···	···
HSC J1443−0007	220.9792	−0.1252	0.89	···	1.29	2.11	0.31	B	···	···
HSC J1501+4221	225.3007	42.3538	0.27	···	1.30	2.78	0.42	A	···	···
HSC J1544+4427	236.2224	44.4637	0.66	···	0.94	1.67	0.47	B	···	···
HSC J1608+4200	242.0651	42.0026	0.64	0.615	1.85	1.56	0.50	B	W	···
HSC J1613+5406	243.4006	54.1154	1.13	0.766	1.29	2.33	0.67	B	···	···
HSC J1618+5449	244.6470	54.8230	0.81	···	1.60	1.56	0.68	B	CAM	···
HSC J1640+4214	250.0049	42.2439	0.66	···	1.97	1.56	0.50	B	···	···
HSC J2208+0446†	332.0220	4.7676	0.27	···	1.60	1.56	0.50	B	W	···
HSC J2212−0018	333.0950	−0.3032	0.91	···	1.31	2.00	0.50	B	F	···
HSC J2236+0240	339.2255	2.6785	0.38	···	1.14	1.67	0.82	B	···	···
HSC J2310+0247	347.5196	2.7999	0.37	0.390	1.75	1.56	0.68	B	RW	6
HSC J2323−0030	350.9419	−0.5105	0.91	···	1.53	2.33	0.67	B	···	3
HSC J2324+0127†	351.0397	1.4579	0.19	0.190	1.94	2.44	0.83	B	W	···
HSC J2331+0000	352.7770	0.0035	0.69	···	1.10	2.00	0.71	B	···	···